

Stellar Echo Imaging of Exoplanets

2016 NASA NIAC Phase I Final Report

Chris Mann, NIAC Fellow
cmann@nanohmics.com

Kieran Lerch, Mark Lucente, Jesus Meza-Galvan, Dan Mitchell,
Josh Ruedin, Spencer Williams, Byron Zollars

Nanohmics, Inc.
6201 E. Oltorf St.
Ste. 400
Austin, TX 78741

Contents

1	Abstract	3
2	Introduction	4
1.1.	Mission architectures	5
2.1	A brief discussion of echo detection and imaging	6
3	Exoplanet detection techniques and stellar echo background	8
4	Technical Analysis	10
4.1	Analytical models	10
4.1.1	Pulse-like signatures	10
4.1.2	Ambient fluctuation signatures	13
4.1.3	Implications of a planet in orbit	16
4.1.4	Mitigating and leveraging the star's geometry	18
4.1.5	Correlation tomography	20
4.1.6	Efficient calculation of stellar echo signals, positive identification, and other considerations	22
4.1.7	The DSCOVR/NISTAR data	23
4.1.8	The CoRoT data	24
4.1.9	The Hubble FGS data	25
4.1.10	Case study: Proxima Centauri	26
4.2	Monte Carlo simulations	27
4.3	System trade study	29
4.3.1	Study of survey missions	29
4.3.2	Study of correlation tomography missions	31
4.3.3	Feasibility of investigating sun-like stars	31
4.3.4	Study of terrestrial planet imaging missions	34
4.4	Laboratory studies	36
5	In Conclusion	36
6	Acknowledgements	37
7	References	38

1 Abstract

All stars exhibit intensity fluctuations over several timescales, from nanoseconds to years. These intensity fluctuations echo off bodies and structures in the star system. We posit that it is possible to take advantage of these echoes to detect, and possibly image, Earth-scale exoplanets. Unlike direct imaging techniques, temporal measurements do not require fringe tracking, maintaining an optically-perfect baseline, or utilizing ultra-contrast coronagraphs. Unlike transit or radial velocity techniques, stellar echo detection is not constrained to any specific orbital inclination. Current results suggest that existing and emerging technology can already enable stellar echo techniques at flare stars, such as Proxima Centauri, including detection, spectroscopic interrogation, and possibly even continent-level imaging of exoplanets in a variety of orbits. Detection of Earth-like planets around Sun-like stars appears to be extremely challenging, but cannot be fully quantified without additional data on micro- and millisecond-scale intensity fluctuations of the Sun. We consider survey missions in the mold of Kepler and place preliminary constraints on the feasibility of producing 3D tomographic maps of other structures in star systems, such as accretion disks. In this report we discuss the theory, limitations, models, and future opportunities for stellar echo imaging.

To resolve an Earth-like planet at the nearest star, Proxima Centauri, it would be necessary to develop a telescope with an optically-perfect baseline of ~2 km. On the other hand, the width of the United States is equivalent to ~14 milliseconds of light travel, a time scale that can be resolved by nearly any off-the-shelf photodetector. By leveraging millisecond-resolved temporal signals from distant solar systems, we can create an interstellar lidar, making it possible to detect and acquire continent-resolution images of distant worlds with existing hardware.

2 Introduction

The recent flood of exoplanet detections is an incredible technological feat that also gives humanity a new perspective of the uniqueness of our place in the universe. Knowing that there are countless other planets in the habitable zones of stars is hardly the end of the inquiry. Steps to perform direct spectroscopic interrogation to understand the composition of these exoplanets and to search for possible signs of life are already underway. However, the inquiry will not end when spectral features are directly and regularly measured. The next challenge will be to *see* these worlds. Directly resolving exoplanets poses several challenges, the first of which is differentiating the trickle of photons reflected by the exoplanet from the ocean of photons coming from the host star. Researchers have approached this problem by investigating complex spatial filters that include starshade coronagraphs, differential spectroscopic techniques, and by considering ultra-large-baseline direct imagers. To exemplify of the scope of the challenge, a spatial resolution of one Earth diameter from an exoplanet at the nearest star, Proxima Centauri, would require a ~2km diffraction-limited telescope, and the requirements get more extreme for more distant stars.

Then there is the fact that all stars have intensity fluctuations over several timescales, from nanoseconds to years. Astronomers seeking exoplanet transits or changes in radial velocity have handled these fluctuations, including stellar variability and spectral jitter, as fundamental limitations. Astronomers seeking to directly image exoplanets have pursued the perfect coronagraph, one where the star's light is removed entirely, but in the process they must delete entire regions of the star systems from their study. In this NIAC study, we considered an alternative: embrace stellar noise and imperfect coronagraphs. We found that, with proper design constraints, these perceived impediments may hold the key to beating the tyranny of the diffraction limit and could enable the first continent-level resolution images of worlds outside of our solar system.

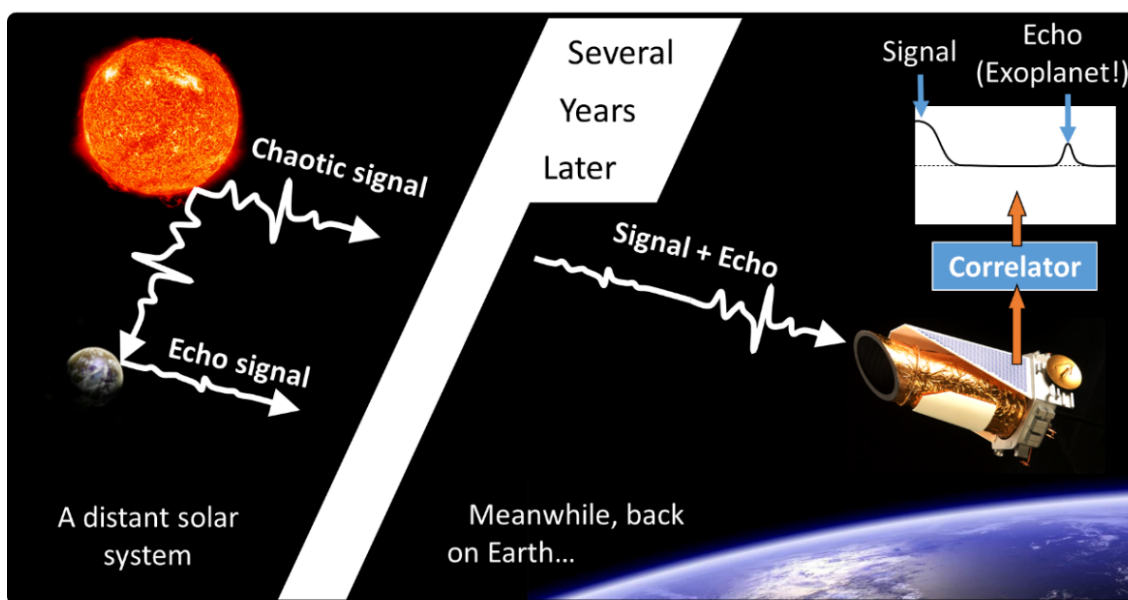


Figure 1. A fluctuation in the intensity of light from a star, as well as its echo from an exoplanet within the system, is captured by a telescope. The signal is digitized and processed by a correlator algorithm, resulting in a time-correlation plot that reveals the structure of the solar system.

We evaluated the feasibility of distinguishing the photons that are from the star from those of the planet by leveraging a temporal effect: the echo. As illustrated in Figure 1, when a star fluctuates, the fluctuation signal takes time to reach the planets in the star system, often many minutes, resulting in a signal and an echo. High-cadence high signal-to-noise measurements can acquire the signal and the faint echo. Temporally resolving the star system, as opposed to spatially resolving the star system, places minimal

requirements on the imaging system and can be achieved with existing technology. Perhaps most tantalizing, the width of the United States is equivalent to ~ 14 ms of light travel, which is a time delay that can be detected by nearly any off-the-shelf photodetector. Consequently, stellar echo techniques may be able to provide continent-level resolution of exoplanets many light years away without requiring multi-km diffraction-limited optically-perfect telescopes.

In this Phase I NIAC program, we evaluated stellar echo techniques and placed bounds on feasibility, determined relevant computational techniques, evaluated the state-of-the-art technology required, and conducted a literature survey. The results are extremely promising for flare stars. Detecting Earth-like exoplanets around Sun-like stars with echo techniques may end up not being practical, but there is still some hope: there is a general lack of high-cadence visible-spectrum data available from our own sun, so the accuracy of our models is limited by this apparent data void. Measurements of the sun from the ground are typically corrupted by atmospheric phenomena and measurements from space are acquired at relatively slow cadences that are optimized for downlink and data storage requirements; therefore, there may still be high variability signals that could be exploited, particularly from atomic emission lines associated with plasma fluctuations.

1.1. Mission architectures

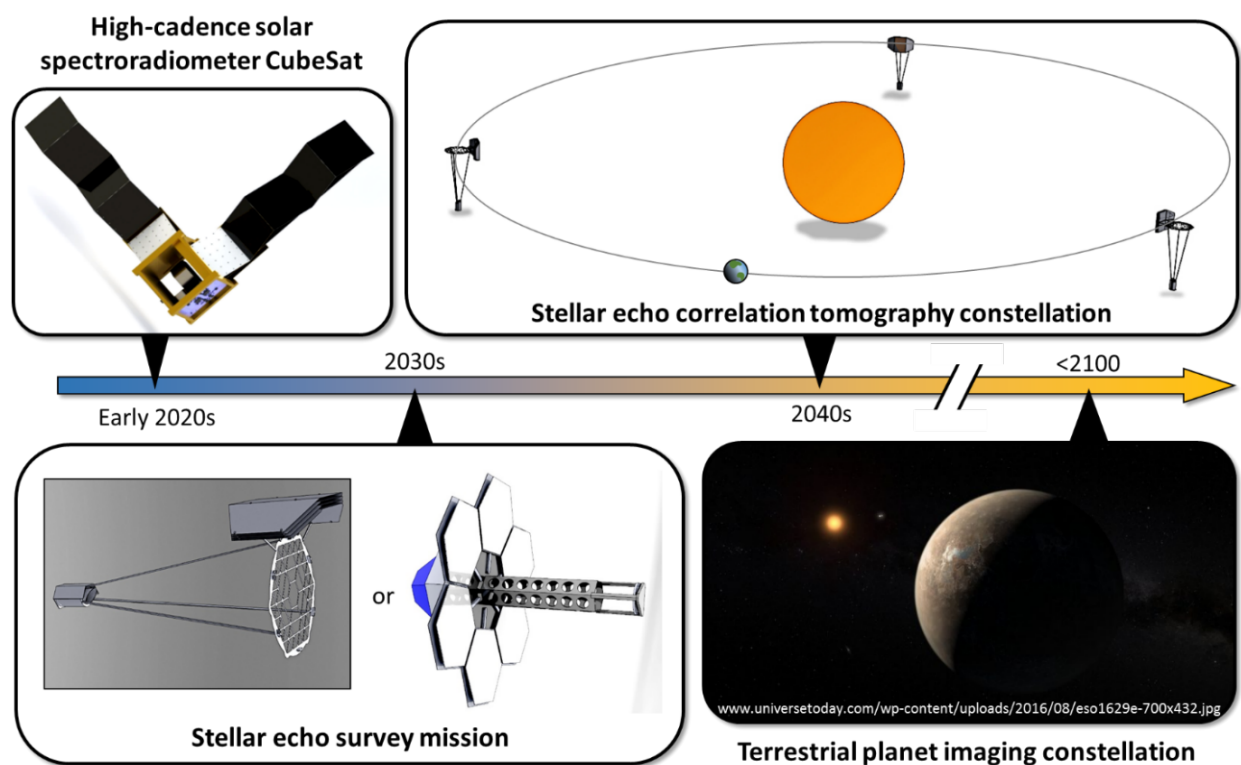


Figure 2. Mission concepts to bring stellar echo imaging to fruition. The first priority is to acquire space-based, high-speed, spectrally-resolved light curves from the sun as a star, in order to determine whether there is sufficient spectral noise to perform stellar echo detection on sun-like stars. In parallel, a stellar echo survey mission will provide the first echoes from flare stars and other high-noise stars. Following successful demonstration of the technique, a subsequent mission would attempt stellar echo correlation tomography to detect Earth-scale exoplanets. If the previous missions are successful, a constellation of high-performance next-generation space telescopes could produce continent-level-resolution echo maps of terrestrial exoplanets.

We envision three distinct stellar echo architectures: exoplanet surveys, echo tomography, and imaging missions where echoes are used in combination with direct imaging methods to produce “super-resolution” maps of exoplanets. Figure 2 illustrates a stepwise implementation strategy. There are two independent early priorities: (1) identifying high-cadence spectral properties of the sun and (2) developing a stellar echo survey mission. The survey mission will emphasize flare stars, so the results will not depend on the sun’s spectral properties. Stellar echo surveys do not require stringent angular resolution, but they do require a large space-based light bucket telescope. Membrane optics and other deployable structures appear to be viable options for this application.

The results from the solar spectroradiometer and survey missions will be used to determine the feasibility of follow-on studies: if the high-cadence solar spectroradiometer successfully identifies highly variable emission lines, then it will be possible to develop a terrestrial planet imager for less-variable Sun-like stars; if the survey mission detects a significant number of exoplanets, accretion disks, or other structures, then it will be compelling to develop a correlation tomography constellation for mapping the high-resolution 3D structure of other solar systems. Table 1 outlines additional scientific benefits to these missions.

Table 1. Mission architecture elements, approximate timeline targets, and the science to be accomplished.

Mission element	Period	Stellar echo goals	Additional science to be accomplished
High-cadence solar spectroradiometer CubeSat	Early 2020’s	<ul style="list-style-type: none"> Determine feasibility of obtaining echoes from sun-like stars 	<ul style="list-style-type: none"> Correlation of microsecond UV/VIS variability with photosphere and coronal events Potential discovery of heliophysics phenomena
Stellar echo survey mission	2030’s	<ul style="list-style-type: none"> Full proof-of-concept, demonstrate feasibility of identifying echoes from flare stars and other noisy targets Determine distribution of echo-relevant star systems 	<ul style="list-style-type: none"> High-resolution asteroseismology survey, substantial signal-to-noise enhancement over CoRoT Exoplanet transit survey Study of interacting binaries Potential discovery of astrophysics phenomena
Stellar echo correlation tomography constellation	2040’s	<ul style="list-style-type: none"> Develop lidar maps of exoplanets and their moons near M dwarfs, ideally spectrally resolved Produce 3D maps of accretion phenomena 	<ul style="list-style-type: none"> Study of flare dynamics on distant stars Potential imaging of stars through rotational timing cross-correlations Detection of non-radial asteroseismology modes
Dedicated terrestrial planet imaging constellation	Before 2100	<ul style="list-style-type: none"> Obtain continent-level resolution of Earth-like exoplanets 	<ul style="list-style-type: none"> High-resolution mapping of stars

2.1 A brief discussion of echo detection and imaging

During the Phase I program, we evaluated several aspects of stellar echo techniques. Here we summarize several of the key points, both positive and negative:

- Spatial resolution is obtained from temporal resolution, not optical interferometry
 - Does not require perfect optical flatness over the baseline
 - Does not require combining beams over large distances
 - Can be operated in survey applications, similar to Kepler
 - Miniscule angular separations are second-scale temporal separations
 - Becomes feasible to detect moon systems

- Does not require ultra-high rejection of the parent star's light
 - Can operate without a stellar coronagraph in survey architectures
 - Can provide super-resolution in telescopes with coronagraphs
- Utilizes reflected light
 - Provides an immediate route towards acquiring spectral measurements
- Is limited by photon counts, requires a very large collection area
 - Cannot collect photons that are not reflected—requires the planet to have a bright albedo
 - Consequently, planets that are discovered are excellent candidates for follow-on spectroscopic studies
- Requires the stars to have a form of noise or intensity fluctuations on a relatively short temporal scale—we have not yet figured out how to force stars to have such phenomena
 - The most common types of stars are red dwarfs, which have consistent and extreme flare events,
 - Some spectral lines, like H- α and Ca II, likely have regular fluctuations
- Is affected by a variety of intrinsic, systematic error sources
 - e.g., fluctuations on the far side of the star relative to the exoplanet may not reach the exoplanet, but can reach our detectors and thereby cause systematic signal de-correlation
 - Some stars may exhibit seismic activity with a well-defined autocorrelation signature that can interfere with the exoplanet detection signal
- Depends on a very stable photometry platform and is sensitive to non-traditional sources of noise
 - Damping of vibrations is challenging in satellite platforms and we discovered that both CoRoT and DSCOVR, the two premiere high-cadence photometry space platforms, have readout noise that can dwarf the signals of interest
- The primary algorithm used is the autocorrelation function, which is well-established
 - Does not require many assumptions about the data
 - As a planet moves in its orbit, the temporal lag changes, requiring a time-dependent autocorrelation analysis
 - Time dependence can be used to quantify orbital parameters
 - May significantly increase the amount of averaging time required to obtain a desired uncertainty
- The location of the fluctuation on the star will influence the autocorrelation signal and will convolve the structure of the star with the planet
 - May requires additional signal averaging
 - One solution is the use of multiple echo detection satellites in order to localize the source of the fluctuation. While this increases the cost and systems management complexity considerably, it also enables 3D correlation tomographic mapping
- Can use cross-correlations between spectral bands to enhance or weight the signal. For instance, while EUV and X-ray emissions will not reflect off exoplanets, they are often associated with other visible spectrum signatures.
 - Systematic correlations and decorrelations between bands can be used to differentiate between direct light and echoed light. However, many of these signatures require a specific phenomenology to function, so each star class is expected to have its own class of phenomena.
- Have not yet explored other means of enhancing the incident signals such as differential polarimetry (scattered light from atmospheres has a polarization dependence) or complementary intensity interferometry techniques that may be able to distinguish between different origins of the light, or provide bounds on the size of the star in order to estimate the geometric deconvolution requirements
- Direct imaging techniques with coronagraphs can isolate the point of light from a given exoplanet, but they cannot resolve the exoplanet themselves.

- Can be used in conjunction with rotational unmixing[1] where time-dependent light curves are extracted and the planet is ‘rotationally unmixed’ in order to assign spectra to individual hemispheres.
- Complementary high-cadence echo data can take advantage of residual starlight and allow extraction of sub-structures within these hemispheres in order to produce images with continent-level resolution

3 Exoplanet detection techniques and stellar echo background

Like transit techniques, the echo detection of exoplanets requires only a single pixel for each star, which makes survey missions viable. However, transit methods fail if a planet’s orbital plane is not exactly aligned with the telescope. Radial velocity methods that measure the changing velocity of a star are an alternative, but these methods fail if the orbital plane is close to perpendicular relative to Earth. In these detection schemes, fluctuations are actually a significant problem: spectral jitter makes radial velocimetry challenging and intensity fluctuations produce false positives for transit techniques. Direct imaging fails for detecting exoplanets that have small angular separation from their host star, where the reflected light signal is actually highest, because they rely on coronagraphs cancelling out the host star’s light. Unfortunately, the coronagraph also blocks all light from an inner angular limit and requires extreme optothermal stability.

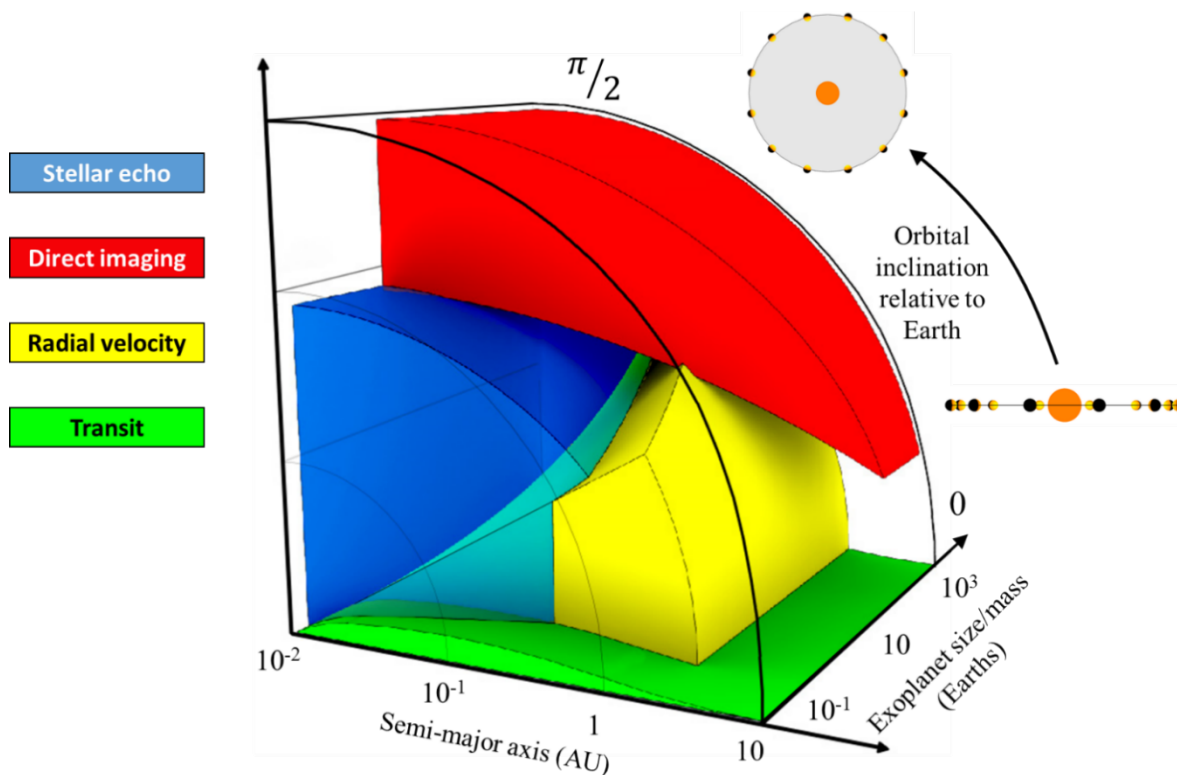


Figure 3. Qualitative detection regimes for stellar echo compared to the most common alternatives. Stellar echo techniques could fill in a missing wedge for detecting exoplanets with small separation. The primary advantage is that stellar echo detection is survey-viable at all orbital inclinations. Note: Direct imaging can image planets in the transiting configuration, but is poorly suited for discovery of exoplanets in this configuration. (Radial coordinate: semi-major axis. Angle coordinate: orbital inclination relative to Earth, where 0 is the transiting configuration, $\pi/2$ is a top-down view. Depth coordinate: exoplanet approximate size/mass)

Stellar echo techniques can detect exoplanets at any orbital inclination, benefit from spectral jitter, and provide orbital data. Echo techniques favor stars having particular temporal properties; however, the detection is not an isolated event like gravitational microlensing, so continued monitoring of the system increases detection certainty. Therefore, stellar echo techniques can help complete the exoplanet census by filling a missing wedge in existing exoplanet detection capabilities.

Figure 3 illustrates detection regimes for stellar echo detection versus other common alternatives. As a survey technique, stellar echo methods can detect a wide range of exoplanet configurations and fills in a missing segment where there are no viable alternatives.

The use of temporal data to detect exoplanets can be traced to a 1971 paper by Rosenblatt,[2] where the transit method is first described, and was refined and re-envisioned as a space-based method by Borucki and Summers in 1984.[3] Notably, the time domain has been heavily exploited by the Kepler mission, which has had unparalleled success in identifying exoplanet systems.[4] Unfortunately, transiting techniques only work if the star system is also in the plane of the Earth, setting a hard limit on the number of viable star systems.

Intensity interferometry techniques also exploit the time domain and have been proposed for exoplanet searches.[5] Intensity interferometry relies on detecting correlated photons and determining the spatial extent of correlated photons by cross-correlating two detectors. While intensity interferometry appears to be very promising for imaging stars and other luminous sources, it faces significant challenges in applications with reflected light.[6] Intensity interferometry is a covariance technique that depends on the fact that thermal sources produce correlated bundles of light within a single emission event. In the visible spectrum, a handful of correlated photons will be produced, but when scattering from the planet, particularly one with an atmosphere, the correlated photons are unlikely to preserve their mode when they scatter towards the telescope. This mode preservation requirement is on top of the already challenging star-planet contrast issue.

As early as 1992, Bromley recognized the potential use of flare echoes to detect exoplanets,[7] though there does not appear to have been considerable follow-on work. In 2009, Clark also evaluated the feasibility of the technique for using pulse-like flare events to detect planets,[8] but was concerned with the “snowflake syndrome,” where each flare is slightly different (both Bromley’s and the present work uses this as an advantage). Clark took an additional step and acquired data from flare stars, but was unable to detect any echo signatures through Earth’s atmosphere.

A related technique is known as imaging ‘light echoes.’ Working at a much larger scale, Sugarman provided a theoretical model for the use of echoes in extended structures, including the use of supernovae to illuminate circumstellar and interstellar media.[9] This technique only works on structures that can be resolved by a telescope, though it has many similar considerations with stellar echo detection.

Throughout this program, we noted a general lack of high-cadence measurements of distant stars, which increases uncertainty of our models. Part of the lack of understanding about microsecond-scale fluctuations on stars appears to be attributed to the Hubble space telescope primary lens spherical aberration. When the Hubble was first repaired, they removed the high-speed photometer to make room for the corrective optics.[10] However, the fine guidance sensor (FGS) remained, and has provided upwards of 40Hz resolution of stellar activity on a few occasions.[11-14] We did not detect any flare activity or echoes in the longest FGS datasets, but we were able to examine the high-speed noise structure of a large star, using the raw data from obtained from the asteroseismology from HD 17156.[15] And while the flare frequency and activity cycles are still disputed, FGS data obtained from Proxima Centauri essentially confirms the feasibility of stellar echo techniques for flare stars, as shown in .[13, 16]

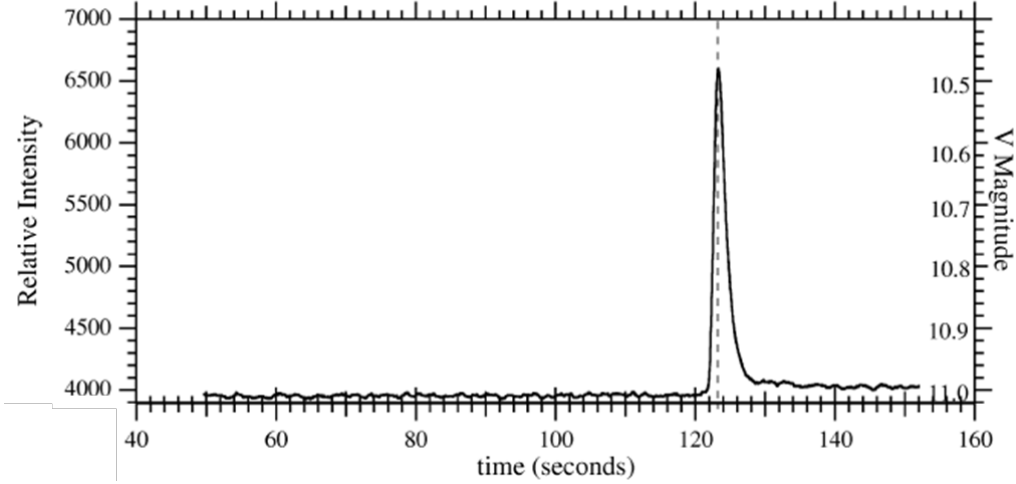


Figure 4. Explosive flare observed at Proxima Centauri by the FGS-3 sensor on Hubble.[13]

4 Technical Analysis

4.1 Analytical models

The core motivation is to produce an ‘interstellar lidar’ where the host star acts as the source, and the resulting signatures echo off the planets in the system—the time lag between the source and the echo event determine the separation between the planet and the host star. The problem is that you can’t coerce stars into producing nice delta-function pulses of light. Instead, by patiently acquiring the signatures from the star system and running an autocorrelation function on them, the echoes can emerge from the noise. We separate this into two classes of signal: pulse-like signatures and ambient fluctuations. Pulse-like signatures include flares, and can be directly identified within the data. On the other hand, ambient fluctuations include other forms of stellar noise, such as local transient events (e.g., plasma instabilities, micro-flares, or thermal fluctuations). These ambient fluctuations can be analyzed through long-duration autocorrelation studies, similar to the FFT techniques applied to asteroseismology data.

4.1.1 Pulse-like signatures

Starting from Bromley’s work, the signal received from a highly localized flare impinging on an exoplanet is given by:[7]

$$I(t) = F(t) + \epsilon F(t - \tau) + Q + N(t)$$

where F is the flare contribution, ϵ is the relative strength of the echo, τ is the echo delay, Q is the mean quiescent photon flux, and N the noise signal. In this form, for a single sharply-peaked flare event of time Δt of magnitude $F = fQ$, Bromley shows that the detection threshold for an exoplanet is approximately:

$$\epsilon_0 \geq \frac{1}{f} \sqrt{\frac{\Delta t}{Q}}$$

If the signal-to-noise ratio is high enough, this can be rewritten in the differential form:

$$\frac{dI(t)}{dt} = \frac{dF(t)}{dt} + \epsilon \frac{dF(t - \tau)}{dt} + N'(t)$$

With N' the noise within the differentiation band, which depends on the processing techniques. In this form, the mean quiescent photon flux falls out of the equation, which has the beneficial effect of removing the background. For instance, the prototypical flare profile has a sharp onset, an exponential tail, and a

long-term post-flare brightening period. The differential signal will have the strongest signature only at the sharp onset, and the echo will reproduce this signature. While this form would be ideal, it essentially requires sufficient signal-to-noise from the echo to directly resolve a single event. Instead, it is typically more practical to consider a high-passed signal, which may or may not be part of the detection hardware.

In general, flares may not be localized, particularly for red dwarf flare stars where the flare can extend over several stellar radii.[13] Consequentially, these sources can emit light over one light-second distances, which is worthy of explicit consideration. In this case, it is necessary to integrate over the region of photon emission. A general form of the intensity received by the detector is given by:

$$I(t) = \int F\left(\vec{r}', t - \frac{\|\vec{r}' - \vec{r}_{tele}\|}{c}\right) + \sum_i \varepsilon_i F\left(\vec{r}', t - \left(\frac{\|\vec{r}' - \vec{r}_{exo,i}\|}{c} + \frac{\|\vec{r}_{exo,i} - \vec{r}_{tele}\|}{c}\right)\right) d\vec{r}' + Q + N(t)$$

Where i is the index of the echoing structure, allowing multiple echo events within the same system. If the source of the echo is extended, such as an accretion disk, the sum can be reformed as an integral over the volume of interest. And because the number of photons scattering from the planet may be in the few-photon-per-second range, it may often be more appropriate to consider the echo contribution as a probability density function that is sampled from, rather than a continuous function.

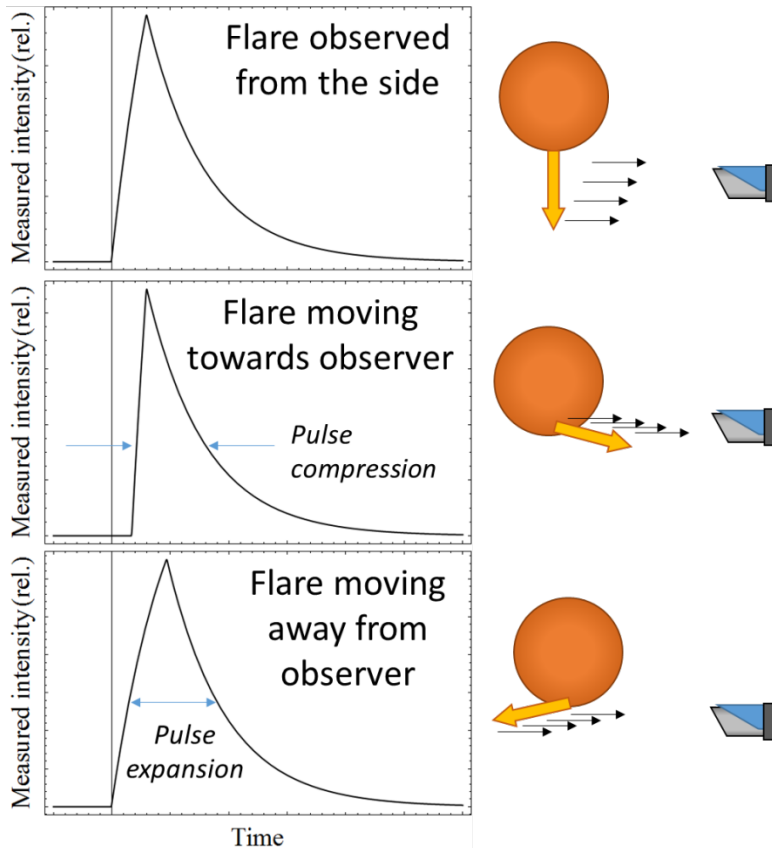


Figure 5. Influence of extended flare structure on pulse shape, assuming an explosive flare with ~5 second full-width half-max and moving at a rate of 0.5c away from its star. The flare emission can extend several stellar radii for some stars. Note that the speed of the planet motion, which is at least ~3 orders of magnitude slower, and typically even slower than that, will have a negligible contribution to the pulse expansion or contraction, so there are no anticipated Doppler-like features from the planetary motion.

Figure 5 shows an example of a (synthetic) extended flare observed from different directions. This effect may cause the exoplanet to echo a slightly different signature from the observed primary pulse. With a large signal-to-noise ratio, the different signatures can be related to their orbital positions, providing additional 3D data about the relative positions of the flare and the exoplanet.

The light reflected from an exoplanet is proportional to its phase law, which is a function that takes into account albedo and its position in orbit. For a Lambertian albedo, the phase law is:[17]

$$\Phi(\alpha) = [\sin(\alpha) + (\pi - \alpha) \cos(\alpha)]/\pi$$

Therefore, when the exoplanet is farthest from the Earth (superior conjunction, $\alpha = 0$), it will reflect the most light. Unfortunately, this is also the position where the Earth cannot observe much of the host star’s activity, so it is necessary to also include the Earth’s view of the star. One approximate means of accounting for this is to consider the mutual view fraction between the star and the planet, which is to multiply the total planet illumination that is visible to Earth, $\Phi(\alpha)$, times the fraction that arrived from a hemisphere of the star that is visible from Earth, $\Phi(\pi - \alpha)$:

$$\Phi(\pi - \alpha)\Phi(\alpha) = [(\sin(\pi - \alpha) + \alpha \cos(\pi - \alpha))(\sin(\alpha) + (\pi - \alpha) \cos(\alpha))]/\pi^2$$

Figure 6 illustrates the relative available echo signal from different inclinations using this reflection fraction.

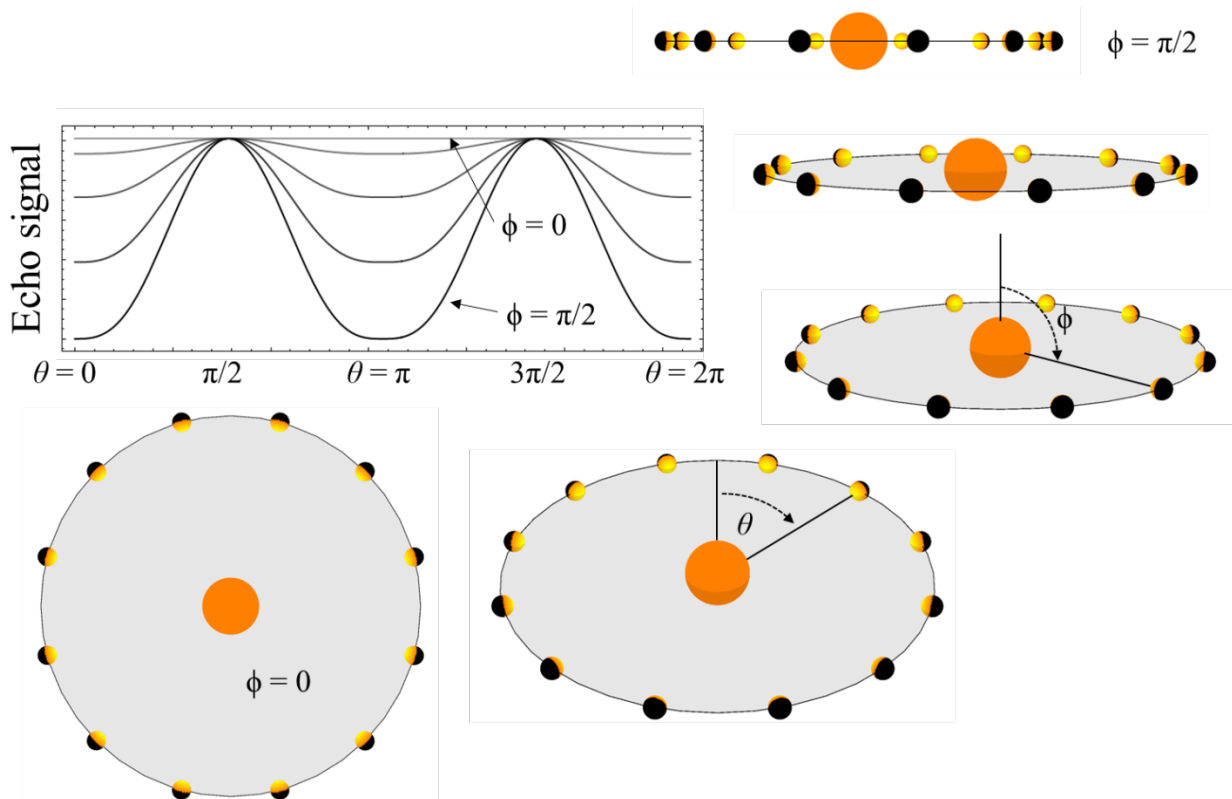


Figure 6. Total signal available for echo detection based on orbital inclination and orbital phase. Top-down ($\phi=0$), there is a consistent signal for all orbital positions. In a transiting-orientation ($\phi=\pi/2$), the signal is maximized when the exoplanet is at its most extreme positions (maximum elongation).

4.1.2 Ambient fluctuation signatures

Without knowing the structure of the stellar intensity fluctuations it is possible, at least in theory, to identify echoes through a relatively simple technique called the autocorrelation. In general, the correlation between two functions f_i and f_j at time lag τ over period T is:

$$C_{ij}(\tau) = \frac{1}{T} \int_0^T f_i(t)f_j(t - \tau)dt \tag{Eq. 1}$$

For $i=j$, this is the autocorrelation function. This can be understood as comparing the data at time t with the data at time $t + \tau$ for every time step in the data series. A larger correlation coefficient indicates a stronger correlation, while a negative correlation coefficient indicates the signal is opposite in magnitude. The normalized, discretized autocorrelation is given by:

$$C(\tau) = \frac{\sum_{i=1}^{N-\tau} (x_i - \mu)(x_{i+\tau} - \mu)}{\sum_{i=1}^N (x_i - \mu)^2} \tag{Eq. 2}$$

where μ is the mean value of x_i with $i = 1, \dots, N$. To provide an example of this data processing technique, consider the data in Figure 7.

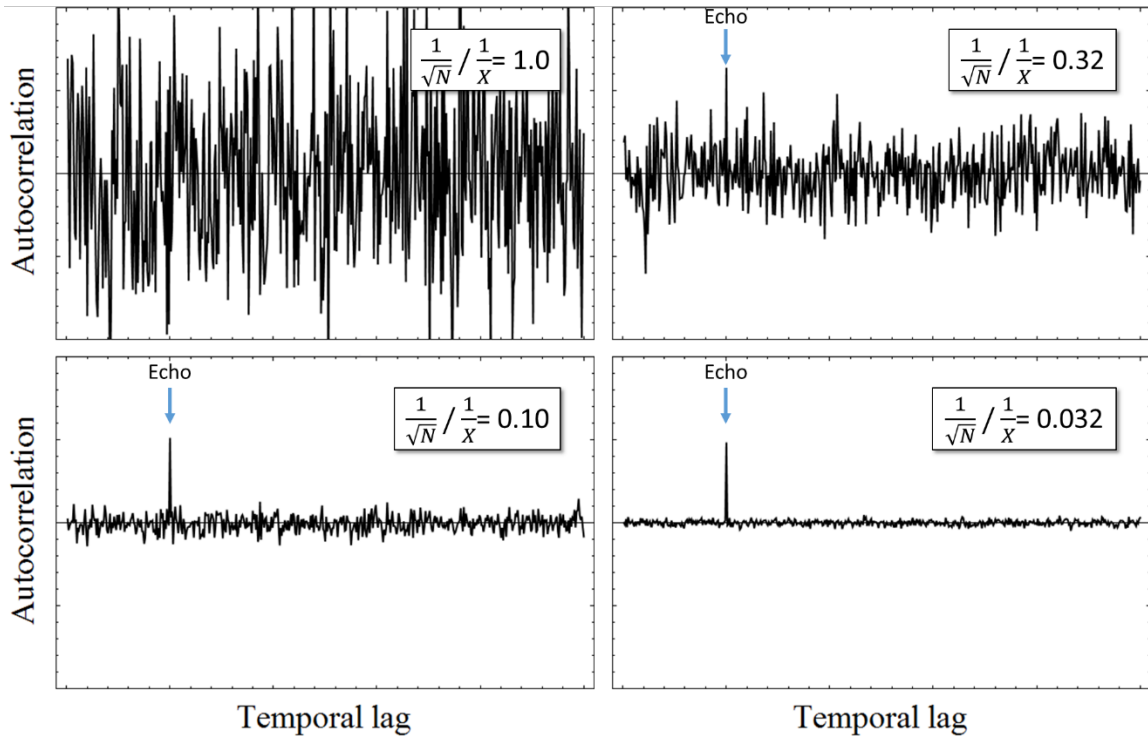


Figure 7. Extraction of an echo of relative strength X from N white noise data points.

The signal-to-noise of the autocorrelation function is determined primarily by the number of samples obtained and converges as $1/\sqrt{N}$, where N is the number of photons received from the star system. To place preliminary bounds on the necessary collection time required to obtain a measurement on an exoplanet with exoplanet-star contrast of ϵ , telescope area A , telescope efficiency η , star intensity reduction due to coronagraph contrast Z , star flux J , detection confidence c , fluctuation frequency ν , and mean relative fluctuation amplitude f , an approximate model is:

$$t \sim (\nu f \epsilon^2 Z J (1 - c)^2 A \eta)^{-1}$$

Table 2 provides a few representative calculations. The time required to detect an echo is minimized by enhancing the coronagraph contrast, maximizing the size of the telescope collection area, and maximizing the available spectral bandwidth, provided that the fluctuations occur across the entire bandwidth (which depends on the phenomenology—a rapidly fluctuating narrow bandwidth can be more valuable than a more stable wide-band measurement). As indicated by these calculations, the stellar echo detection technique is directly viable for detecting exoplanets that are too close to their host star to be resolved by direct imaging techniques. For wider separations or smaller planet-star contrast ratios, a coronagraph becomes necessary. However, it is not necessary to have a state-of-the-art 10^9 blocking power coronagraph to produce useful echo data that cannot be obtained through other means.

Table 2. Preliminary values from nearby systems using an 88nm wide V-band filter, 70% combined telescope and detector quantum efficiency, and a 10m space telescope, assuming the planet is in quadrature.

Detection goal	Star mag	Time between flares	Flare magnitude	Coronagraph contrast	Planet albedo	Planet distance (AU)	Planet/star contrast	Time for 1-sigma
Hot Jupiter at Proxima Centauri	11.13	31hr	100%	None	0.3	0.015	$\sim 10^{-4}$	26 days
Jupiter at 0.5AU Proxima Centauri	11.13	31hr	100%	10^5	0.5	0.5	$\sim 10^{-7}$	119 days
Earth-sized Proxima b	11.13	31hr	100%	10^5	0.35	0.05	$\sim 10^{-7}$	352 days
Hot Jupiter at Lacaille 8760	6.7	27hr	10%	None	0.3	0.015	$\sim 10^{-4}$	3.9 days
Jupiter in habitable zone at Lacaille 8760	6.7	27hr	10%	10^4	0.5	0.3	$\sim 10^{-7}$	23 days

To resolve Earth-like planets, we anticipate needing to resolve ~ 50 ms events, which means that the target operating rate is ~ 20 -50 Hz, a tremendous cadence for traditional telescopes that typically integrate for a minute or more. The photon counting noise follows Poisson statistics, so for every N photons received, we expect a counting error of \sqrt{N} photons. To calculate the noise within a given sample, it's necessary to consider the photometry of the stars, which may vary considerably. Generally speaking, however, they are referenced to a standard set of magnitudes within specific bands, as outlined in Table 3.

Table 3. Absolute photometry for several visible passbands, selected from Bessell.[18]

Filter band	λ_0 ($\Delta\lambda$) nm	Flux density for mag = 0.00 W/m^2-hz
B	440 (97)	4.26×10^{-23}
V	550 (88)	3.64×10^{-23}
R _c	640 (147)	3.08×10^{-23}

The brightness difference between a mag 0 star and a mag m star is given by:

$$\frac{F_m}{F_0} = 10^{-0.4m}$$

The energy in a photon is given by $E = hc/\lambda$, or $\sim 6.61 \times 10^{-19}$ J at the center of the V band. The frequency bandwidth conversion from wavelength bandwidth, $\Delta\lambda$, for a photon centered at wavelength λ_0 is:

$$\Delta f = c\Delta\lambda / (\lambda_0^2 - (\frac{\Delta\lambda}{2})^2)$$

For a magnitude m star, the photon flux (number of photons arriving per second per m^2) within a sub-band of width $\Delta\lambda$ in the V band is:

$$J(\lambda_0, \Delta\lambda, m) = \frac{I_V 10^{-0.4m} \lambda_0 \Delta\lambda}{h \left(\lambda_0^2 - \left(\frac{\Delta\lambda}{2} \right)^2 \right)}$$

where I_V is the flux density within the V band (from Table 3). For Poisson counting noise with a collection area of A , the signal-to-noise ratio (SNR) for a sampling frequency f or sampling time t is:

$$SNR = \sqrt{JA/f} = \sqrt{JAt}$$

The signal to noise for 20 ms cadence and 1 μ s cadence is plotted for different telescope sizes and star magnitudes in Figure 8 and Figure 9. The reason for considering 1 μ s cadences is described in the following section related to cross-correlating the star shape with the planet echoes.

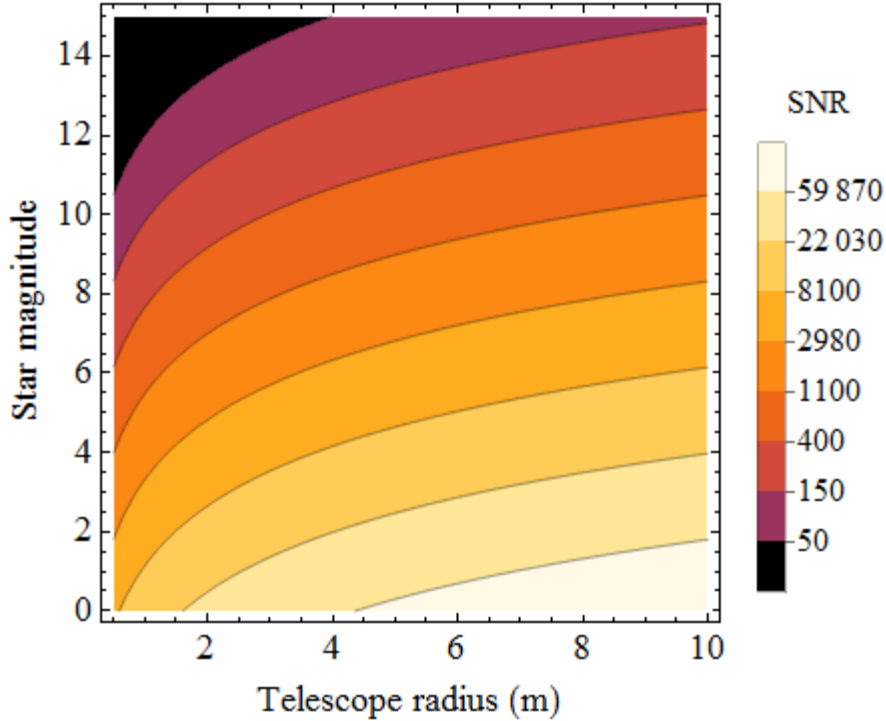


Figure 8. Optimal signal-to-noise ratio plotted as a function of star magnitude and telescope size assuming a 30 nm sub-band of the V band at a 20 ms cadence.

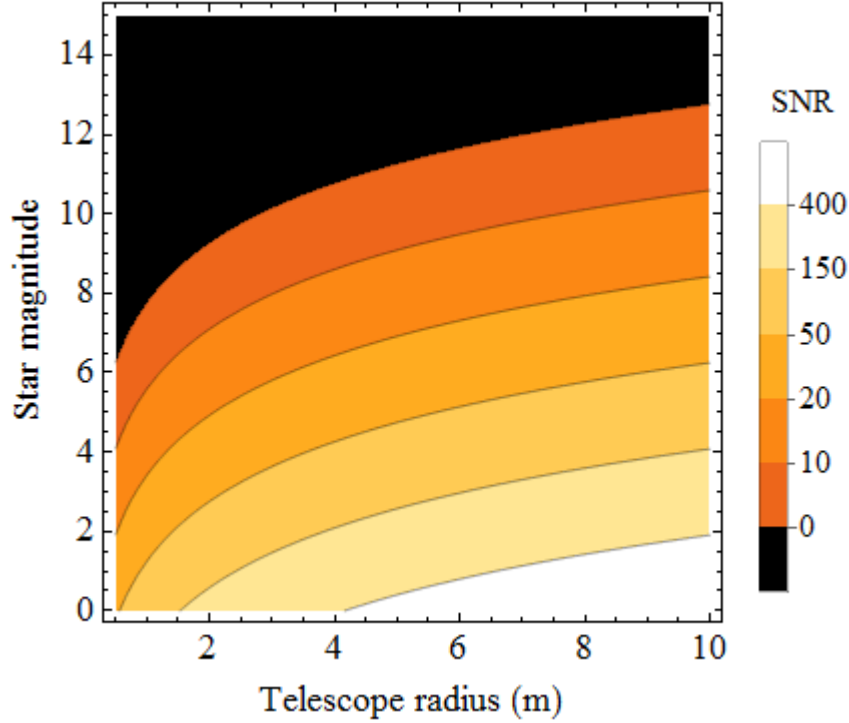


Figure 9. Optimal signal-to-noise ratio plotted as a function of star magnitude and telescope size assuming a 30 nm sub-band of the V band at a 1 μs cadence. This timescale is useful for cross-correlation localization of flares, but is likely impractical for other applications.

4.1.3 Implications of a planet in orbit

The autocorrelation described previously is used to describe stationary processes. However, for most orbits, the correlation function changes as a function of time. Therefore, it is necessary to evaluate a time-dependent autocorrelation. One way of handling this is to utilize a moving window function (similar to a Gabor transform):

$$C(\tau, t) = \frac{\sum_{i=1}^{N-\tau} W(i, t)(x_i - \mu(t))W(i + \tau, t)(x_{i+\tau} - \mu(t))}{\sum_{i=1}^N W(i, t)^2(x_i - \mu(t))^2}$$

where $W(i, t)$ is a window function centered at time t and evaluated at position i and $\mu(t)$ is the mean value of $W(i, t)x_i$, with $i = 1, \dots, N$. The width and shape of the window function can impact the resulting data—the window size will ideally be large enough to provide at least one sigma of standard deviation. A few standard window options are the boxcar or rectangular window, the triangular window, the Welch or parabolic window, the Hamming window, and so forth. These are regularly used in signal processing, such as reducing finite sample effects from a Fourier transform. The result of the window function is to limit the extent of the data processed and (excepting the boxcar window) to weight the data at the center of the window more heavily. Figure 10 shows an example of a time-dependent autocorrelation for a simulated planet with a nearly perpendicular orbital plane relative to Earth.

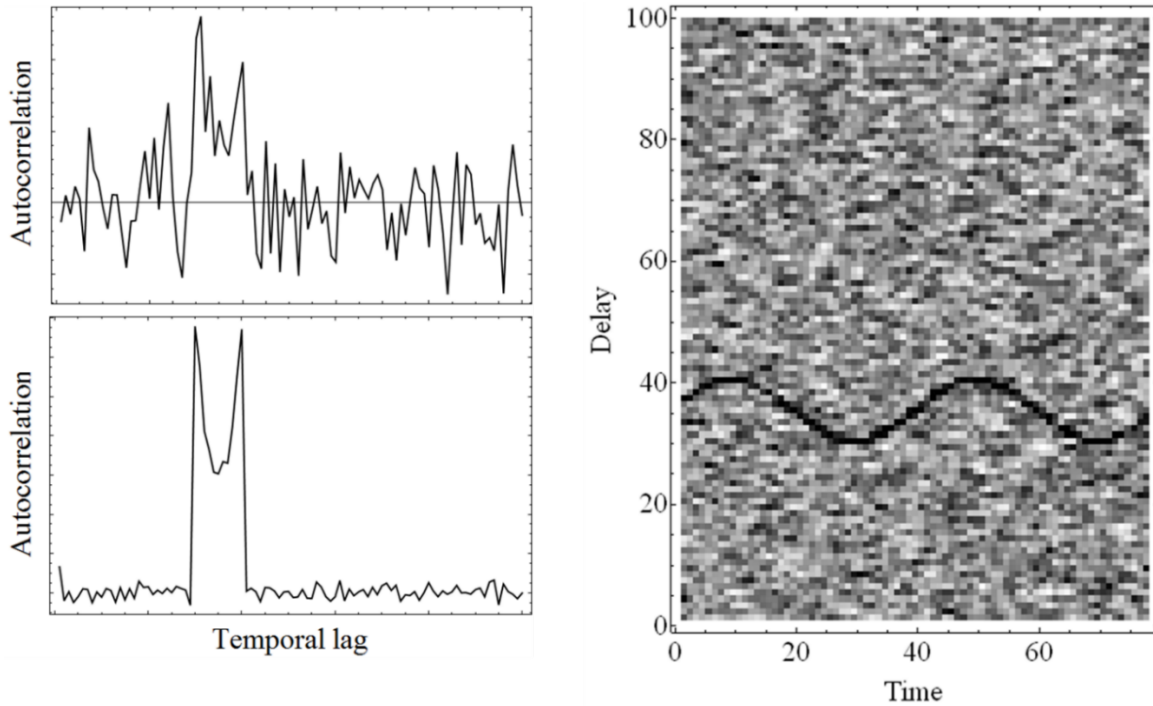


Figure 10. (Top Left) Autocorrelation from a signal with a varying delay term. It is challenging to isolate the signal from the standard autocorrelation. (Bottom Left) A comparable signal after averaging for two orders of magnitude longer reveals structure within the autocorrelation, but does not reveal its behavior. (Right) A time-dependent autocorrelation taken from the noisy data used on the Top Left readily reveals the periodic signal.

Detection probability depends on several factors including the albedo, orbit, and stellar properties. Figure 11 shows examples of the ideal signal and intensity as a function of orbital parameter for two eccentricities. These plots were generated by numerically solving Kepler’s equation, which is a transcendental equation that cannot be directly solved, then calculating the echo lag as a function of time in the orbit. The signal intensity was scaled by the inverse square falloff as well as an approximate echo view factor term described in §4.1.1. Using this technique, the ‘ideal’ time-dependent autocorrelation can be determined for any orbit.

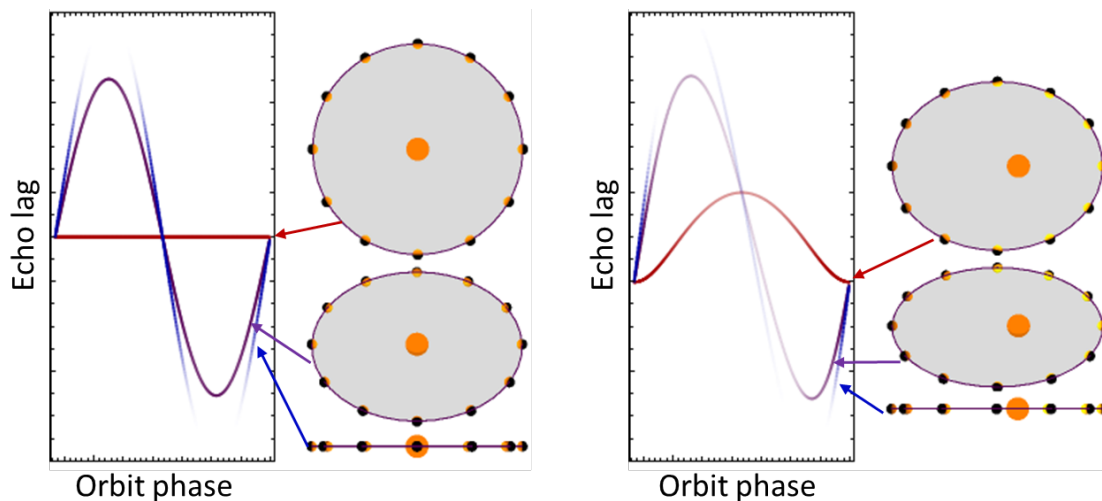


Figure 11. Idealized time-dependent autocorrelation curves as a function of orbital inclination and orbit. The signal intensity is scaled by the approximate view factor of the planet and the view factor of the side of the star that the planet is facing. (Left) Circular orbit and (Right) an eccentric orbit.

There are often a number of orbital positions that can be satisfied by a given time lag, or even time-dependent autocorrelation curve. For instance, a sine-like signal could be a circular orbit viewed at an angle or an elliptic orbit viewed top-down. To further constrain the orbit, consider the star as a point source at \vec{x}_{star} and the planet is a delta-function scatterer at $\vec{x}_{exoplanet}$, such that the time lag is given by:

$$\Delta t = \frac{1}{c} (|\vec{x}_{exoplanet} - \vec{x}_{star}| + |\vec{x}_{Earth} - \vec{x}_{exoplanet}| - |\vec{x}_{star} - \vec{x}_{Earth}|)$$

where c is the speed of light. Assuming that the star is at the origin, and assuming a coordinate system where Earth is directly along the z axis at distance d , then the expression simplifies to:

$$\begin{aligned} \Delta t &= \frac{1}{c} (|\vec{x}_{exoplanet}| + |d \hat{z} - \vec{x}_{exoplanet}| - d) \\ &= \frac{1}{c} \left(\sqrt{x_{exo}^2 + y_{exo}^2 + z_{exo}^2} + \sqrt{x_{exo}^2 + y_{exo}^2 + (z_{exo} - d)^2} - d \right) \end{aligned}$$

Under a coordinate transformation of $z' = z_{exo} - d/2$, $2a = c\Delta t + d$, $\eta = d/2$ this becomes the more familiar form of a Cartesian coordinate ellipsoid, (more specifically, a spheroid), which is defined by:

$$2a = \sqrt{x^2 + y^2 + (z + \eta)^2} + \sqrt{x^2 + y^2 + (z - \eta)^2}$$

Having this analytical form makes it easier to perform error analysis, for instance, and to take advantage of the various known relations for an ellipsoid. Another way of writing the potential positions of the exoplanet in orbit relative to our detectors is given by the implicit relation:

$$\frac{x^2 + y^2}{a^2 - \eta^2} + \frac{z^2}{a^2} = 1$$

It is also clear that the exoplanet will be quite close to the star (relative to the size of the spheroid, which extends past the detectors), so a detection limit sphere can further constrain the position of the exoplanet. Figure 12a illustrates the spheroid and inverse square law falloff. Figure 12b illustrates triangulating the positions of the exoplanet using multiple detectors with a large separation.

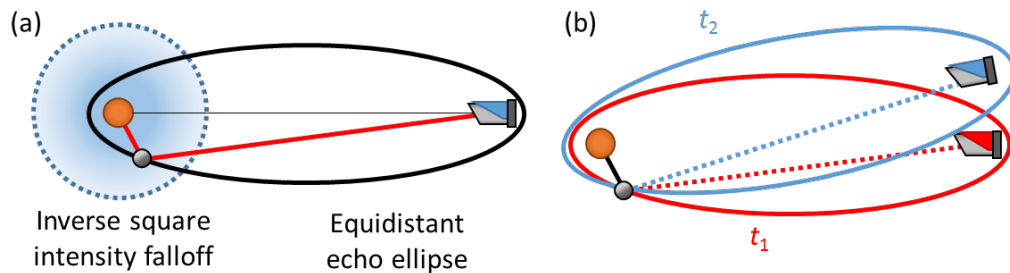


Figure 12. (a) For a given time lag, there is a spheroid of equivalent travel time such that the position of the planet cannot be immediately determined. This is cropped by an inverse square law intensity falloff, where planets are unlikely to be detected outside a given threshold. (b) With multiple detectors, it's possible to triangulate the position of the echo without tracking the full orbit.

4.1.4 Mitigating and leveraging the star's geometry

One of the challenges with stellar echo detection is the influence of the geometry of the star on the signals received. Stars are not point sources and flares and fluctuation events will occur in multiple locations. Each event will have a different time delay to the exoplanet, resulting in several different delays instead of a

single star-exoplanet delay. Consequently, the autocorrelation function will have the effect of convolving the shape of the star with the exoplanet, reducing the signal-to-noise.

Fortunately, one solution to this problem enables “echo correlation tomography.” By including additional detectors, it is possible to distinguish not only the echoes, but also to localize the sources of fluctuations on stars to a single hemisphere, and possibly even higher precision. Identifying the location of the fluctuation removes one significant source of systematic error, which is when the star has a flare on a side of the star that the planet cannot see, but our detectors can see. Figure 13 illustrates this point. By utilizing two detectors, the cross-correlation lag between the detectors can localize the origin of the event.

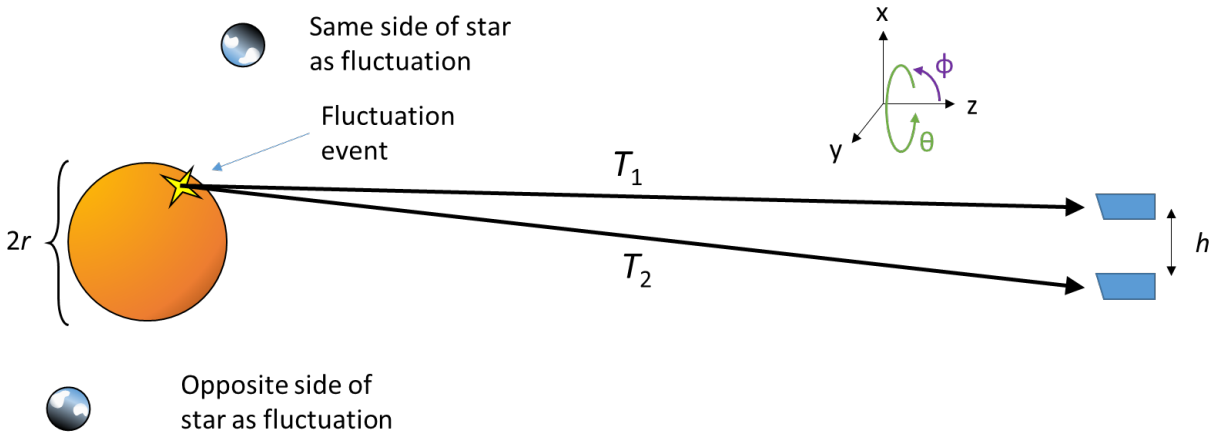


Figure 13. A fluctuation event on a star can be picked up by exoplanets on the same side of the star, but not those on the opposite side. By using two detectors, the timing delay can be used to determine on which side of the star the fluctuation occurred, allowing individual fluctuation events to be mapped to, at least, a hemisphere.

Quantitatively, if the star is distance L away (along the z -axis), the two detectors are separated by distance h , and both detectors are centered relative to the star, then

- Detector 1 position: $\vec{D}_1 = (\frac{h}{2}, 0, L)$
- Detector 2 position: $\vec{D}_2 = (-\frac{h}{2}, 0, L)$
- Coordinate of fluctuation on star: $\vec{P} = (r \cos(\theta) \sin(\phi), r \sin(\theta) \sin(\phi), r \cos(\phi))$
- Delay in arrival at the detectors: $\Delta t = (|\vec{D}_2 - \vec{P}| - |\vec{D}_1 - \vec{P}|)/c$

Once the norms are written out, the terms under the square root are not easily combined. However, because $L \gg r, h$, both terms are readily expanded as a Taylor series, canceling out the majority of terms. The resulting delay between detectors is:

$$\Delta t = \frac{h r \cos(\theta) \sin(\phi)}{c(L - r \cos(\phi))}$$

Figure 14 shows the calculated maximum timing delays for stars at different distances from Earth, using two detectors separated by 1AU, assuming the star is the same size as the sun. Consequently, the relative timing uncertainty between detectors should be $\leq 1 \mu s$ in order to provide useful cross-correlation values for tomographic and localization purposes.

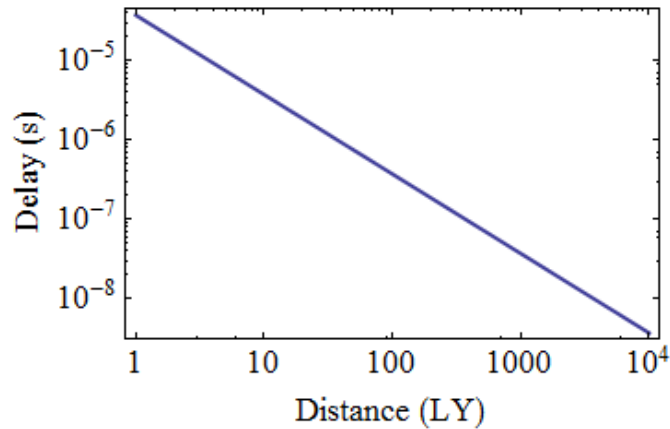


Figure 14. Maximum timing delay between two detectors separated by 1AU observing a sun-sized star at different distances from Earth.

4.1.5 Correlation tomography

Cross-correlation of fluctuation lags opens a framework for echo correlation tomography, where 3D data is extracted from the star system. While the emphasis of this program is on detecting exoplanets, other extended structures in star systems, including accretion disks, can be probed as well. And with multiple detectors, a 3D density map is possible, though challenging.

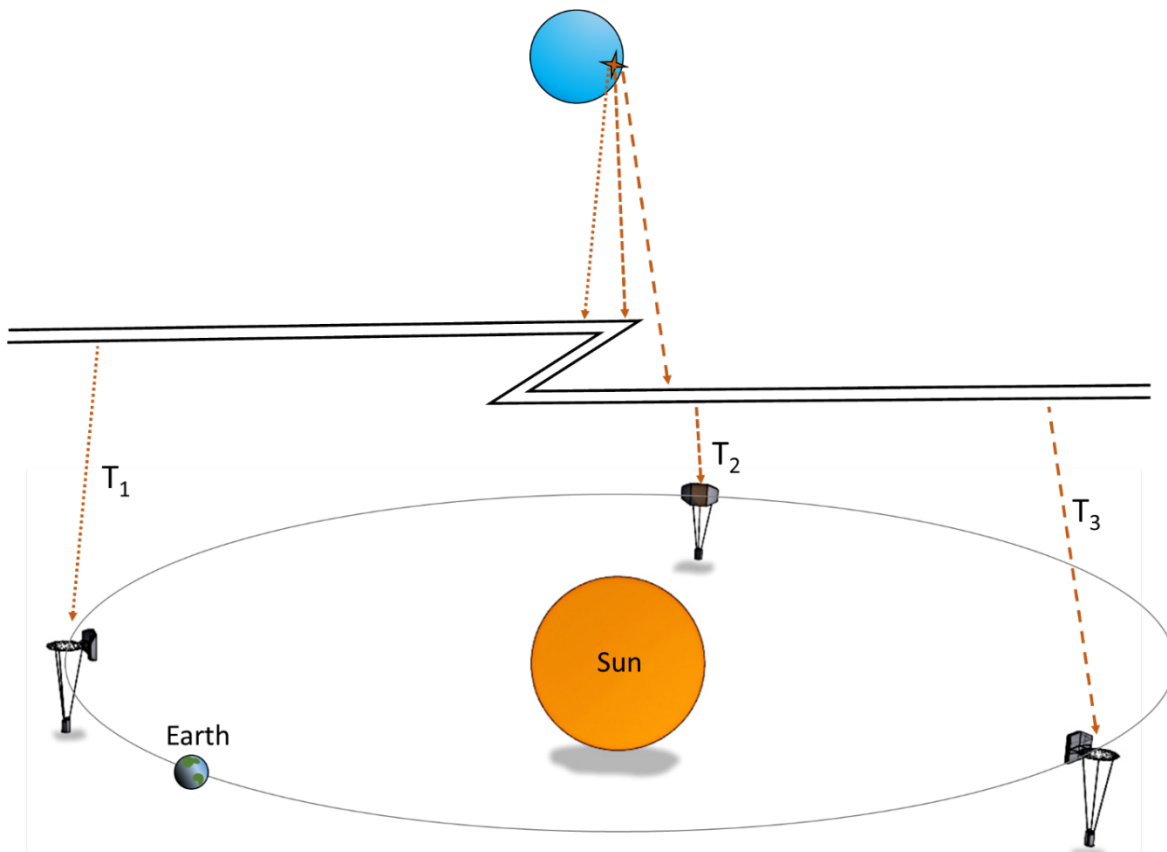


Figure 15. Placing detectors into different phases of Earth’s orbit, for instance, will create a sufficiently large baselines to triangulate the position of a given fluctuation on a star many lightyears away. The STEREO spacecraft have analogous orbits, so there is an established precedent for deep-space telescopes.

The reference architecture for echo correlation tomography comprises three detection sites in an Earth-like orbit, similar to the STEREO orbits, as illustrated in Figure 15. The Earth-Sun L3, L4, and L5 Lagrange points are examples of a large-baseline system that may be useful. A maximum 1 μs relative timing delay puts constraints on the allowable timing jitter in the circuits, which must be highly accurate, but not outside the realm of modern clock technology. Another point worth mentioning is that if one of the telescopes is not in the same orbital plane as the others, its position can be ‘corrected’ by altering the timing delay computationally.

The tomography reconstruction kernel would be a spheroid with one focus at the source of the fluctuation and the other focus at the telescope. The spheroid would be weighted by an inverse-square falloff, an approximate scattering phase law, and the relative signal-echo view factor. Detailed exploration of echo correlation tomography remains as a future task.

4.1.5.1 Localization of sensors and synchronization of time [Case study]

Consider the large-baseline example of sensors located at the Sun-Earth Lagrange points of L3, L4 and L5. How do these sensors know their location? For the sensors at L4 and L5, the Sun and Earth locations will be highly visible and can be used with ephemeris data to determine rough positioning. Additional periodic signals, such as those of pulsars[19] have been explored for determining the position of a single spacecraft location and relative location between spacecraft.[20] However, it is necessary to synchronize the sensor clocks from across the solar system, which requires several considerations.

The benefit of increasing the baseline between instruments comes with a cost of increased complexity. Consider a scenario where there are sensors positioned at the Sun-Earth Lagrange points L3, L4 and L5. These points form a roughly equilateral triangle distributed around the sun on the Earth’s orbital path, with L3 point being directly on the opposite side of the Sun from the Earth. Since each Lagrange point is located on the Earth’s orbital path, each one is located one Astronomical unit (AU) from the Sun. The distance between sensors (e.g. each leg of a hypothetical equilateral triangle) is $2 \cdot \text{AU} \cdot \cos(\pi/6)$. Now consider that an observation is made and each sensor must communicate the time they noted the observation in order to properly place the observation in space. The time for a speed-of-light message to travel from one sensor to the next is equal to the distance between the sending and receiving sensors divided by the speed of light, or $2 \cdot \text{AU} \cdot \cos(\pi/6)/c$ which is roughly 14 minutes. However, clock synchronization between sensors must also consider the impact of special and general relativity. Note that as in our simplified example, the sensors at the L3, L4, L5 point are all rotating around the Sun synchronously with the Earth, so they ideally experience no relative motion. In practice, objects placed at the L4 and L5 points are stable in that they maintain station, while those at the L3 point must expend energy to maintain their position, and this is usually accomplished with a Lissajous trajectory about the L3 point. This Lissajous trajectory will cause some variation in velocity between the L3 and the L4,L5 sensors, but there are many possible Lissajous trajectories and the amplitude would generally be small. However, there is a definite fixed difference in the gravity experienced between L3 and the L4,L5 points, and that has an impact on the sensors’ perceived time due to general relativity. The sensor at L3 experiences less gravity than the sensors at L4,L5 which are closer to Earth, so that the clock of the sensor at L3 runs more slowly. The equation for time dilation due to gravity is:

$$T = \frac{T_0}{\sqrt{1 - \frac{2GM}{Rc^2}}}$$

with, T the relative period, T_0 the observed period between events, G is the gravitational constant, M is the mass of the object creating the field, R is the mean radius, and c is the speed of light.

In our case, the clock at L3 runs 1.00000000022195 times faster than clock on the sensors at L4,L5. Stated another way, the clock on the sensor at L3 gains 1.917 microseconds per day vs. the sensor at L4,L5 due to gravitational time dilation. Fortunately, this value can be pre-calculated and compensated in actual measurements.

4.1.6 Efficient calculation of stellar echo signals, positive identification, and other considerations

Performing an autocorrelation is a relatively common calculation that is relatively straight-forward to code, and is included as a stock function in programs like Mathematica (CorrelationFunction). However, the identification of exoplanets requires more than a simple 1D autocorrelation, because for the majority of orbits, a time-dependent autocorrelation is required. Additionally, the orbit will exhibit periodicity, so it would be advantageous to take advantage of this periodicity to improve the signal-to-noise.

The primary methods for exploiting periodicity include Fourier transforms and data folding. Because the signal is periodic, a Fourier transform seems natural, but the signals will appear to be peak-like, similar to a Dirac comb. From Monte Carlo simulations, we found that there was a slight increase in the power spectral density from FFT analysis, but its structure was often ambiguous. Data folding is an alternative to FFTs and complementary to time-dependent autocorrelation, where the data is assumed to be periodic, but no assumptions are made about the structure of the data (i.e., the signals are not decomposed into sines, so they can have more complex shapes). The data folding process is to take a signal, say x_1, \dots, x_N . Then, for a period T , there will be a maximum of T data bins and likely fewer, as there will be some form of windowing, kernel smoothing, or binning. For a simple single data point in each bin, the signal at time x_i and x_{i+T} are included in the same bin, resulting in all data that matches that periodicity being averaged out. The random errors will converge as $\sim 1/\sqrt{N/T}$, but this assumes that the correct period has been chosen. Unfortunately, selecting the correct orbital period *a priori* is impossible unless the period has already been detected through other techniques, so the primary source of error will be systematic uncertainty.

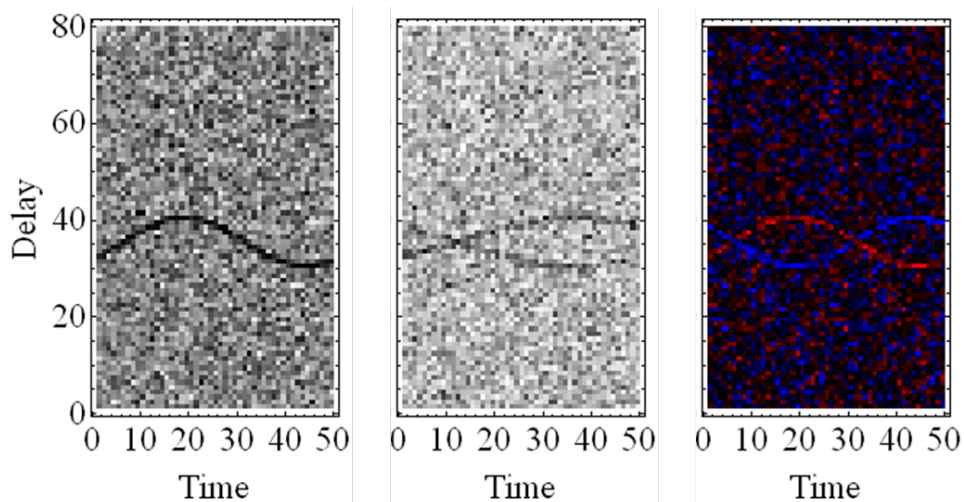


Figure 16. (Left) A periodic signal found by data folding. (Middle) The same signal, but folded at half the period shows a clear Lissajous structure. (Right) By weighting every other period of a Lissajous with opposite signs, then summing them, real signals will reveal their phase dependence, while false signals will average to zero.

Fortunately, we identified at least one means of performing an orbital period search that appears to be reliable and robust to several forms of false positives. Figure 16 illustrates two verification methods for. There are two key ideas to support the parameter search: (1) periodic, systematic noise that can masquerade as a signal will have higher harmonics in the lag axis, while an echo from a planet will not, and (2) the

signal will exhibit even and odd harmonics in the time axis if the periodicity is off by exactly an integer or half-integer multiple of the period, resembling a Lissajous plot, while noise will not preserve the time-domain harmonics.

When performing an orbital period search, it quickly becomes apparent that many of the calculations are redundant. In particular, a large number of products will be calculated for every candidate orbital period. Instead, by pre-computing all of the products, different data folding periods can quickly be summed even by a scripting program like Python. To summarize in pseudo-code:

```
LagMatrix = [LagMax-LagMin][NumPoints-LagMax]
```

For each i in range NumPoints:

 For each Lag in range LagMin to LagMax:

$$\text{LagMatrix}[\text{Lag}][i] = x_i x_{i+\text{Lag}}$$

To calculate the non-normalized autocorrelation, sum all points in the array for a given time lag. To calculate a period-folded dataset at period T , list-convolve the array at each time lag with a Dirac comb, or delta function array, $d[i] = \sum_k \delta(i - kT)$. By replacing the delta function with a window function, this is a straight-forward way to produce a filtered dataset. Other kernels are also viable, including $d[i] = \sum_k (-1)^k \delta(i - kT/2)$, which results in data that is shifted by a half-period being subtracted, rather than added, to the signal, producing datasets like that shown on the right side of Figure 16.

Because the signals of interest are relatively high-speed, the first step in the data processing is typically to high-pass filter the signals. This removes a large number of effects including stellar rotations, detector drift, and thermal background drift. It's conceivable that this high-pass filter could be included on the pixel itself, such as an AC-coupled CCD or a ROIC with tailored electronic bandpass elements on each pixel, but this may remove data useful to asteroseismologists. Recognizing that the signals of interest are relatively faint echoes against a large background, we evaluated another pre-processing step that brings the signals into a comparable magnitude. The goal is to magnify extremely small signals and reduce the magnitude of extremely large signals. One function that performs this task, while maintaining a 1-1 mapping of the data, is the square root (because the data has been high-pass filtered, it's important to use a sign-preserving version of the root). For instance, a signal that was 1/100 becomes 1/10, while a signal that was 100 becomes 10. The order of magnitude separation between these signals goes from 10^4 to 10^2 . Other root laws are also options, such as the 6th root. This preprocessing step was found to be exceptionally useful in some simulations, and useless in others. More evaluation of this processing step is required to understand the best ways to use it.

4.1.7 The DSCOVR/NISTAR data

The Deep Space Climate Observatory, or DSCOVR, satellite is positioned at the Earth-Sun L1 point. One of its instruments, the National Institute of Standards and Technology Advanced Radiometer (NISTAR), acquires high-cadence radiometry of Earth. We attempted to determine the approximate magnitude of stellar fluctuations at Earth using the photodiode data from the NISTAR instrument, but discovered that its autocorrelations are plagued by what appears to be harmonic noise, as shown in Figure 17. While there may be a way to account for this, we moved on to other tests in the interest of time.

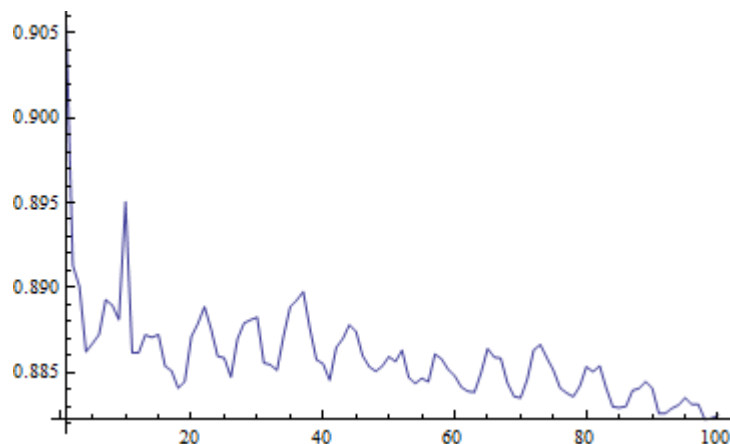


Figure 17. Example of an autocorrelation plot from the NISTAR photodiode data.

4.1.8 The CoRoT data

The CoRoT space mission, launched on 2006 December 27, was developed and is operated by the CNES, with participation of the Science Programs of ESA, ESA's RSSD, Austria, Belgium, Brazil, Germany and Spain. As an asteroseismology probe, CoRoT obtained thousands of hours of stellar intensity signals from high-magnitude stars. CoRoT has a relatively small aperture (27cm) compared to the requirements of stellar echo measurements, and a back-of-the-envelope calculation suggested that a hot super-Jupiter would be just barely outside the detection threshold of stellar echo techniques. However, given the large volume of data, it was worth investigating and practicing the signal processing on real data. We analyzed the time-dependent data for dozens of the longest CoRoT datasets and in the process developed many of the techniques described previously. During this analysis, we found that preprocessing the data with high-pass square-root filters prior to performing time-dependent autocorrelation analysis was effective in revealing structure within the signals, but the majority of the structure that we identified appeared simultaneously in multiple datasets. We concluded that the structure that we observed was likely caused by other factors, like orbital influences or electronic noise. With further analysis, it may be possible to subtract these factors, but there was a diminishing return for the time remaining in the program.

Figure 18 shows an extreme example of digital noise. The autocorrelation revealed that there was a minor intensity spike every 32 seconds, which happened to be the exact readout cadence of a nearby FPA. This kind of crosstalk would not necessarily be apparent in most analysis techniques, indicating that echo techniques may be sensitive to different types of noise than other measurements. Figure 19 shows a less noisy signal. Most stars we examined were somewhere between these two results. The double-hump structure was present at similar scale in nearly all measurements, indicating that it was likely an instrumentation artifact and not a property of stars.

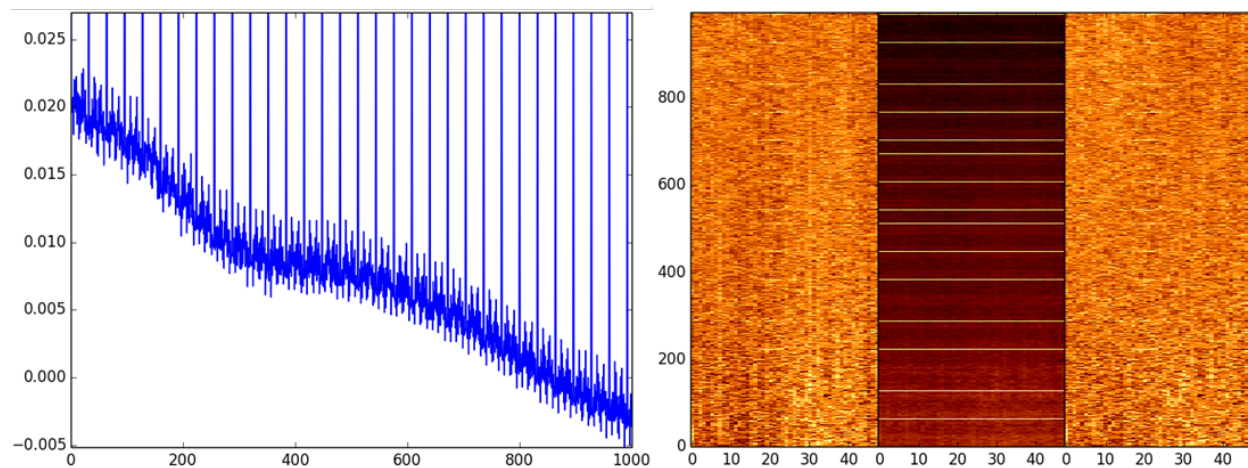


Figure 18. Results for HD 180642, CoRoT target 8393. (Left) Autocorrelation and (Right) three different processing techniques for the time-dependent autocorrelation.

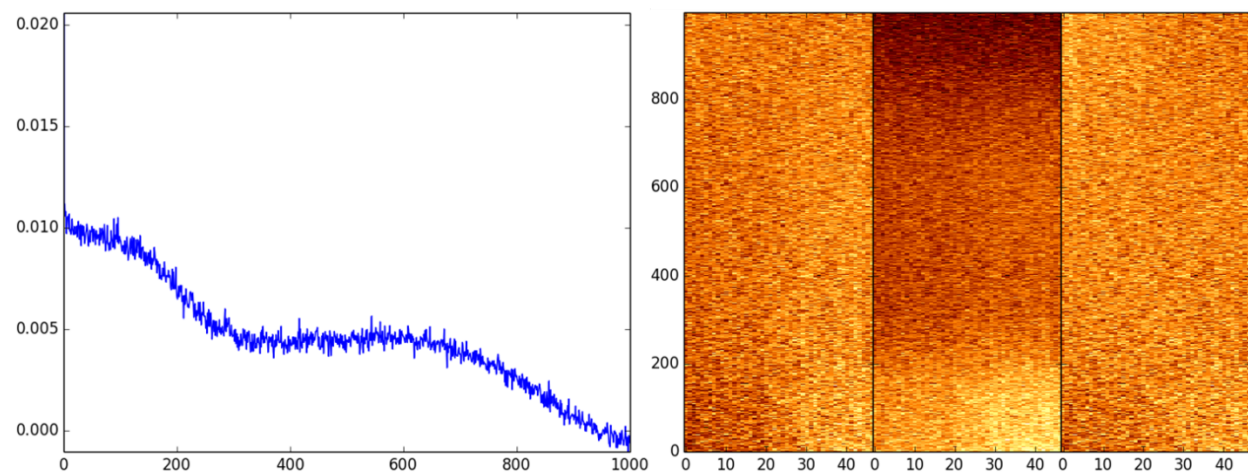


Figure 19. Results for HD 171835, CoRoT target 8394. (Left) Autocorrelation and (Right) three different processing techniques for the time-dependent autocorrelation.

4.1.9 The Hubble FGS data

We were able to access and test the raw data from the longest continuous data run from the Hubble FGS data sensor, which corresponded to a particularly exciting measurement. For 10 days, Hubble stared at a single star for an asteroseismology measurement of star HD 17156.[15] Additionally, the star is known to have a transiting exoplanet on a highly eccentric orbit that results in the planet coming close enough to the star to be interesting for echo studies. The measurement cadence of 40Hz was high enough to attempt to identify high-cadence fluctuations from the star. Figure 20 shows the processed data. The streaks in the windowed time-dependent autocorrelation indicate that the sensor has several additional high-frequency components, but this measurement represents the best available data for stellar echo purposes that we were able to identify. To fully understand this particular data set, it would likely require at least three of the exoplanet’s orbital periods of data (~66 days). Additionally, there was little expectation of significant fluctuations from HD 17156, given that is more massive than our own sun, though only longer duration analysis would be able to confirm this.

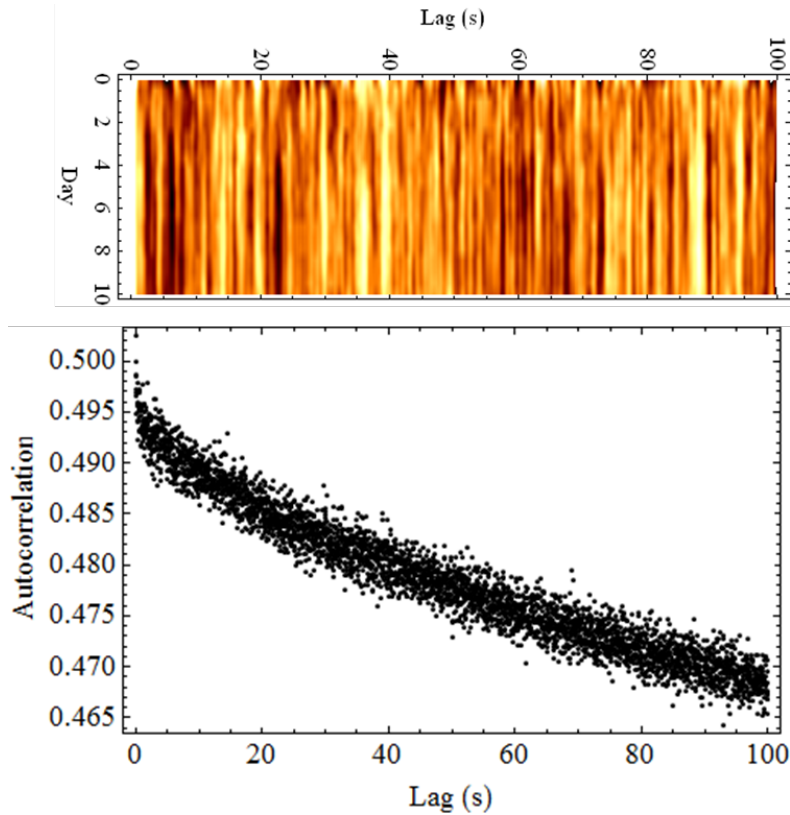


Figure 20. Autocorrelation of the data obtained by Gilliland *et al* of HD 17156.[15] (Top) Time-dependent autocorrelation and (Bottom) the total autocorrelation from the measurement.

4.1.10 Case study: Proxima Centauri

Proxima Centauri is the closest star to the Earth, at a distance of ~4.24 LY.[11] As a red dwarf and flare star with a reported exoplanet,[21] it is an extremely interesting candidate for evaluating the stellar echo technique. Furthermore, Proxima Centauri’s Ca II line appears to be particularly inconsistent,[22] which would have additional benefits for ambient echo-based techniques. Table 4 summarizes some relevant known parameters.

Table 4. Parameters for the Proxima Centarui case study.

Parameter	Measured value	Citations
Magnitude	11.13	Lurie <i>et al</i> [23]
Distance	4.24 LY	Benedict <i>et al</i> [11]
Explosive flare magnitude and frequency	-0.6mag every 31 hr [Walker] “Strong flare” every >27 hr [Cincunegui]	Walker[16] Cincunegui <i>et al</i> [22]
Standard flare magnitude and frequency	-0.05mag every 5 hr [Walker] “Weaker flare” every >18hr [Cincunegui]	
Explosive flare rise time	~1.4sec	Benedict <i>et al</i> [13]
Proxima b orbital parameters	Semi-major axis: 0.05AU Eccentricity: <0.35 Period: 11.186 days	Anglada-Escude <i>et al</i> [21]

Based on the flare measured by Benedict *et al* shown in Figure 4, [13] the relative intensity spiked by ~65%, from ~4000 to ~6600 within ~1.4 sec. Figure 21 illustrates the telescope requirements for detecting an exoplanet at Proxima Centauri with high confidence using stellar echo techniques. Given the uncertainty in flare intensity and frequency, these represent preliminary values. If a given band, such as H- α , contributes more heavily to the flare by, say, an order of magnitude, which is not unreasonable to consider, then all of the integration times can be reduced by an order of magnitude by selecting the H- α band for the study. Phenomenology plays a key role in the signal analysis, so follow-on analysis will be key to fully constraining the feasibility.

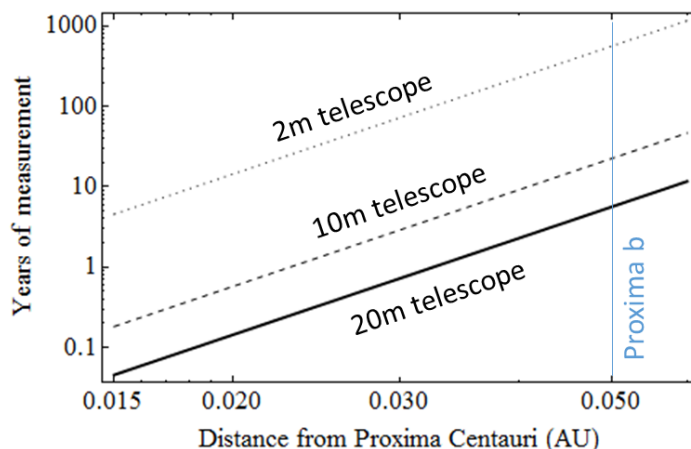


Figure 21. Telescope size and detection time for different distances from Proxima Centauri. Assumes no coronagraph, Jupiter albedo and radius, 65% flare magnitude, 31 hours between explosive flares, 200nm bandwidth, 70% efficient telescope, and a 75% detection confidence.

4.2 Monte Carlo simulations

To evaluate the validity of the approach, we have prepared a variety of simulations. All of the simulations require a noise model, and until we have access to realistic star fluctuation data, all of the fluctuations we evaluate will have inherent assumptions. One type of assumption is the temporal structure of the fluctuations—what Fourier components are most pronounced? Presently, we are assuming white noise processes due to the simplicity in producing the simulations.

To evaluate the influence of the spatial extent of the star, we considered an ideal star that has multiple sources simultaneously emitting and calculated the resulting autocorrelation function (Figure 22). With enough averaging, the impact of multiple emitters will average out, but this can take a considerable amount of time—ideally, the technique would be robust to this source of systematic noise. We will be updating this model to account for multiple detectors in order to evaluate the ability to localize sources of noise in order to enhance the signal-to-noise. Additionally, we will soon be including higher levels of detail into the time-dependent models, such as the orbital phase dependence on the received echo signals.

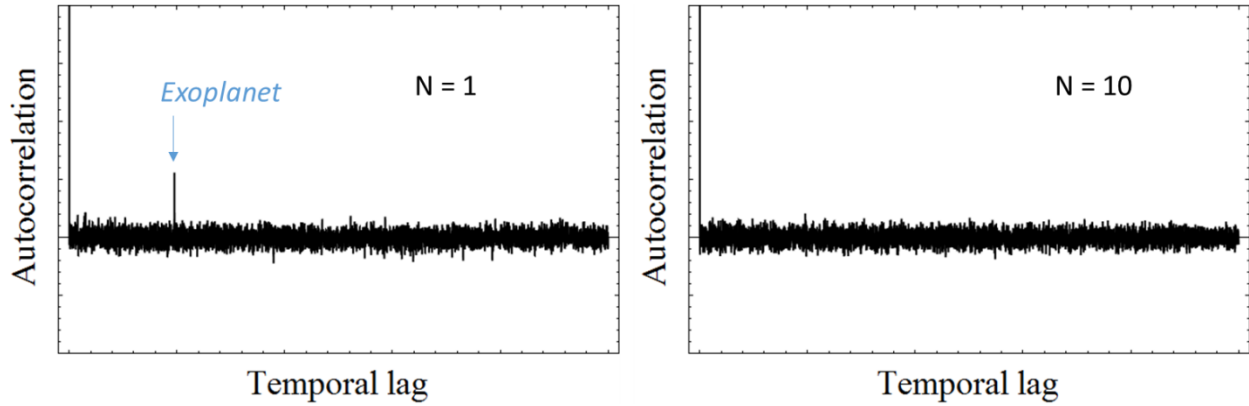


Figure 22. The influence of multiple independent emitters on the surface of a star. (Left) For a single emitter, the exoplanet can be readily isolated. (Right) With 10 emitters, the exoplanet can no longer be identified through the noise without additional averaging.

We also developed a flare-based model, which represents a sparse collection of sharp-onset, high-magnitude signals, instead of a consistent baseline of small fluctuations. Local events, such as convection cells, provide minute-by-minute fluctuations, but are also ubiquitous and likely average each other out, so we’re unlikely to implement a convection model.

As an explosive flare model, we use a linear-onset with an exponential decay term, mimicking the behavior in Figure 4. Poisson noise is added based on the intensity of a “pure signal” which is created by summing a background intensity, a time-dependent flare intensity, and a faint flare echo signal.

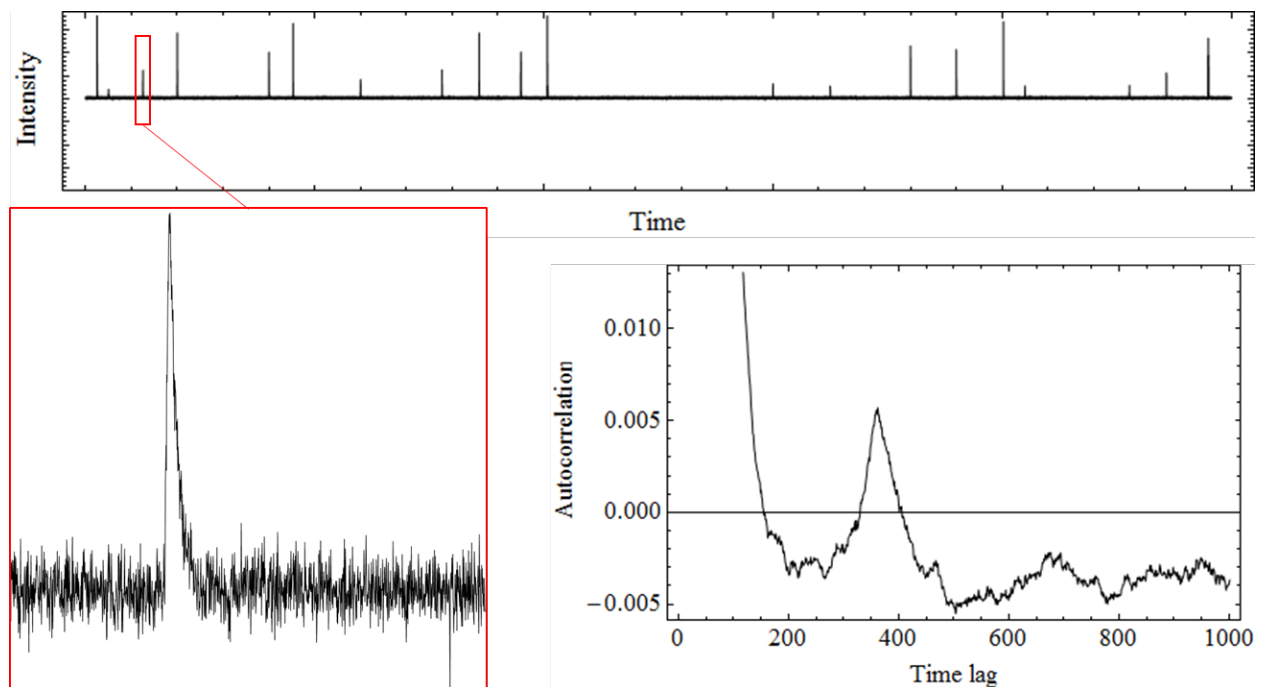


Figure 23. Example of synthetic data from the flare model. (Top) A series of flares produce high magnitude spikes ranging from 10% to 90% of the mean quiescent flux intensity. (Bottom Left) These flares echo at a level that is below the shot noise level. (Bottom Right) Resulting autocorrelation plot of the entire time series reveals the echo, which occurs 360 samples after the initial flare.

4.3 System trade study

As described in §1.1, we envision three distinct stellar echo architectures: exoplanet surveys, echo tomography, and imaging missions. Timelines for space telescope studies are often on the order of two to three decades. The Kepler space probe launched March 7, 2009, and its roots can be traced to a 1971 paper by Rosenblatt[2] and was first envisioned as a space telescope by Borucki and Summers in 1984.[3] Given the reduced cost of access to space since the 1980s, it is conceivable that future missions will be transitioned more rapidly, but a minimum timeline of a decade is still realistic. Based on the advances anticipated over the next decade, we foresee several new options for space telescopes. For instance, the anticipated launch of the 6.5m James Webb Space Telescope will provide a pathway towards ultra-large deployable mirror structures.

4.3.1 Study of survey missions

A stellar echo survey mission requires a large light bucket with a large field of view. Because the stellar echo does not require extreme angular resolution, the optical surfaces are not required to be exceptionally flat, relaxing fabrication requirements.

Another major factor is scintillation. The atmosphere moves at a high speed, so in order to average out the effects of the atmosphere, it's necessary to either operate outside of bands that are heavily influenced the atmosphere, operate with significantly large collection areas that average out the effects of the atmosphere, or simply to operate outside of the atmosphere. From the work of Dravins *et al.*,[24] we have determined that acquiring measurements in the atmosphere will be a significant problem. For high-speed measurements, less than 100 μ s cadence, it is possible to obtain useful data, but around 300 μ s, the 'inner scale' of atmospheric turbulence turns on and influences the signal. This means that 'aperture averaging,' or a very large collection aperture, is needed in order to average over multiple scintillation cells.

From follow-on work by Dravins *et al.*,[25] they showed that multiple telescopes can be used to get around this problem more readily than with a single large telescope, because they sample different, uncorrelated portions of the atmosphere. They describe the scintillation-noise amplitude decreasing with telescope diameter as $D^{-2/3}$, while the noise amplitude decreases with $1/\sqrt{\text{Number of telescopes}}$, so a factor of 10x reduction in noise requires either a 1000x increase in telescope area (30x diameter) or 100 small telescopes. For cost reasons, the large number of small telescopes is almost always preferable, but this makes time synchronization more challenging. Furthermore, because the highest signal-to-noise events are brief flares, having a staring array with near 100% up time maximizes the probability of success. While it is likely possible to demonstrate the feasibility of stellar echo techniques by studying high-magnitude flare stars using very large Earth-based telescopes, a formal survey mission will require a space telescope that can stare for months on end, much like the Kepler mission.

Transit-based exoplanet detection occurs on timescales of minutes to hours, and is therefore amenable to long exposure and readout times. Because of this, the combinations of the FPAs and optics used in current exoplanet survey missions are not capable of producing the SNR required for stellar echo detection and imaging. For example, the CHEOPS survey telescope is designed such that the brightest stars in its field of view just reach saturation at the end of its 60 second exposure time; reduce that exposure time by a factor of one hundred or more, and the 100 ke/pixel wells will be dominated by Poisson noise.

Data rate limits on most FPAs reduce the number of pixels that can be read, which is problematic for wide-field survey instruments looking at many stars. The FPA will most likely need to be of a CMOS type, which are only recently reaching the performance requirements for space telescopes. Examples of science-grade CMOS detectors are shown below.

I. TAOS II (e2v VEGA image sensor CIS113)

- CMOS
- can be butted together on three sides to construct a large FPA
- one 5 x 5 pixel block can achieve 10,000 fps, “but even faster is possible”

Parameter	Value
Pixels (H x V pixels)	1920 x 4608
Pixel size (µm x µm)	16 x 16
Image area (mm x mm)	73.728 x 30.72
Number of outputs	8
Time to read and readout one complete row or half row	130 µs
Well depth	19 ke ⁻ (15.5 ke ⁻ linear)
Readout noise (e ⁻ RMS)	2.3 typical, 5.0 max
QE @ 800nm	0.50

II. JUICE (e2v SIRIUS image sensor CIS115)

- CMOS
- like other e2v CMOS, individual regions of interest can be read at higher framerates

Parameter	Value
Pixels (H x V pixels)	1504 x 2000
Pixel size (µm x µm)	7 x 7
Number of outputs	4
Time to read and readout one complete row	66.25 µs
Readout rate	6.2 Mpixel/s (typical), 10 Mpixel/s (max)
Well depth	33 ke ⁻ (27 ke ⁻ linear)
Mean readout noise (e ⁻ RMS)	5
QE @ 650nm	0.90

The design approach to flat fielding and undersampling error could have a large impact on the number of simultaneous observations that can be made as well as the SNR; for example, a typical approach is to defocus the optics, but this decreases photon flux on each pixel, as well as increasing the readout time. A possible compromise is to use optics without a central obscuration (such as membrane optics), which can be defocused such that the PSF just overfills a single pixel. This eliminates undersampling error, without as great a loss of SNR, and none of the loss in temporal resolution associated with defocusing. Used in combination with precision guidance systems and calibration, flat field error may also be minimized.

Additional important differences are a massive amount of data that the higher temporal resolution will generate, the minimization of the relative importance of dark current, and the greater importance of readout noise.

We evaluated different large-area space telescope technologies that may be viable, and membrane optics appear to have the highest TRL for ultra-large-area space-based telescopes, though there is still a significant demonstration gap. The highest TRL system we are aware of is DARPA’s MOIRE telescope,[26, 27] which provides a route towards a large-area chromatically-corrected diffraction membrane telescope, but is lacking a demonstration in space. Figure 24 illustrates a first draft of a membrane telescope with a sun shade.

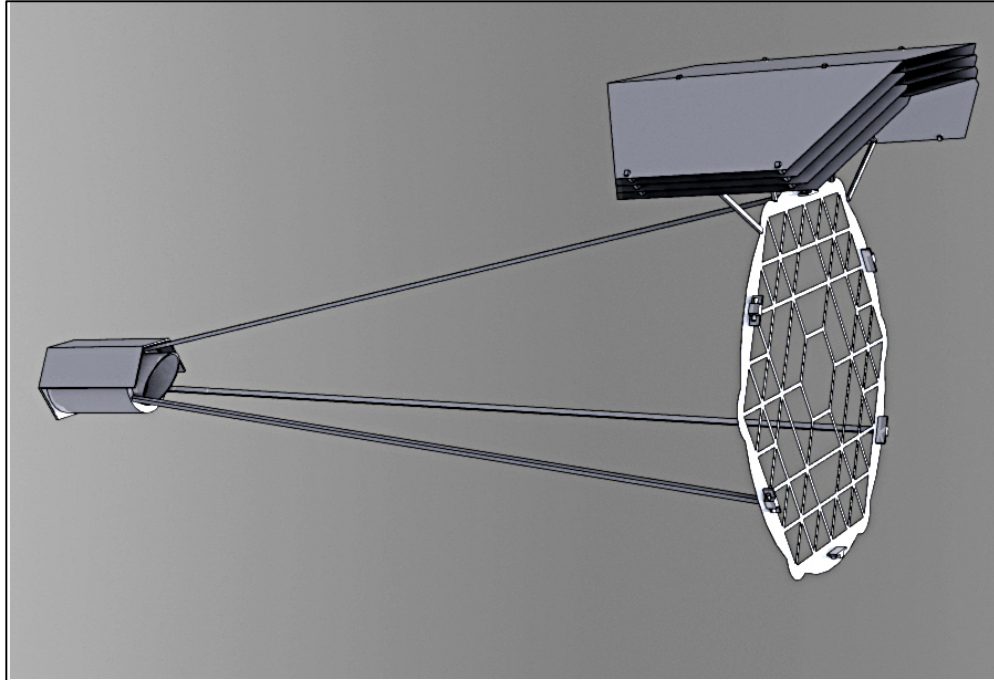


Figure 24. Concept for a membrane-optic telescope.

Alternatively, the James Webb space telescope (JWST) is expected to demonstrate large-area deployable mirrors. The optical quality of these mirrors is substantially higher than the expected requirements for stellar echo, which primarily requires a light bucket, but many of the lessons that will be learned from JWST can be applied to the deployment of other large space telescope structures.

4.3.2 *Study of correlation tomography missions*

As we studied the influence of multiple flare locations on the same star during the Monte Carlo simulations, it became apparent that localizing the source of the flares may be necessary for high-performance signal analysis. §4.1.5 describes the basic framework required to determine the position of the flares. While the purpose of this study was to evaluate the feasibility of identifying exoplanets, a multi-baseline mission opens the door to ‘correlation tomography’ mapping of distant star systems. This includes planets and their moons, but also includes extended structures like dust, accretion disks, and distributions of debris. We did not pursue specific studies within the Phase I program, but anticipate that echo correlation tomography mapping could be an exciting area of study in the future.

4.3.3 *Feasibility of investigating sun-like stars*

Exoplanets may be detectable for a variety of orbits around flare stars, but what about exoplanets orbiting Sun-like stars?

During a solar flare, it has recently been discovered that the total energy radiated by the flare is actually highest in the visible spectrum, but is dwarfed by the star’s background. In particular, there is more intrinsic variation in the star caused by acoustic waves and solar granulation.[28] For heliophysicists attempting to study solar flares, having a varying background is an impedance, but is extremely promising for producing consistent high-cadence variation for stellar echo measurements. Unfortunately, the majority of solar research is performed over longer timescales—the limiting factors are often the hardware selected to readout the data from the detectors. With sufficient motivation to understand the high-speed solar phenomena, existing detectors could easily perform the measurements.

We see a high-cadence solar spectroradiometer as an essential step prior to fully investigating sun-like stars. In particular, individual emission lines are known to be more variable, but down to what timescale? We approached this question in two ways: envisioning a CubeSat spectroradiometer and attempting to measure the sun-moon echo.

4.3.3.1 *A high-cadence CubeSat spectroradiometer*

The goal of a high-cadence spectroradiometer is to determine the power spectral density as a function of wavelength. We started with a worst case S/N analysis, shown in Table 5.

Table 5. Worst-case S/N analysis.

Parameter	Value	Product
Visible spectral irradiance in space	530 W/m ²	
Slit area	5 μm x 1 mm	2.65 μW
Exposure time	1 μs	2.65 pJ
Efficiency of monochromator	0.30	0.8 pJ
Quantum efficiency of focal plane array	0.25	0.2 pJ
Energy per 550 nm photon	0.369 aJ	540,000 photons
Number of bands	1000	540 photons/band
Readout noise	50 e ⁻ RMS	SNR: 10.8

Thus, high-speed spectrometry can be photon-starved even when staring at the sun. Without changing any of these values, however, it is possible to drastically improve the situation by coupling more light into the system with a lens or concentrator. A small COTS achromat/asphere positioned such that its image plane coincides with the entrance slit, would restrict the field of view rather than the coupled power.

Parameter	Value	Product
Visible spectral irradiance in space	530 W/m ²	
½” Lens area (90% clear aperture)	1 * 10 ⁻⁴ m ²	53 mW
Exposure time	1 μs	53 nJ
Efficiency of monochromator	0.30	16 nJ
Quantum efficiency of focal plane array	0.25	4 nJ
Energy per 550 nm photon	0.369 aJ	10 billion photons
Number of bands	1000	10 million photons/band
Readout noise	50 e ⁻ RMS	SNR: 200,000

It’s likely that a COTS lens will need an iris or filter to limit the power coupled into the system. We produced a preliminary design for a high-cadence CubeSat spectroradiometer using the following COTS lenses:

- Edmund Optics #49664 (aspherized achromat, input coupler)
- Thorlabs AC050-008-A (achromatic doublet)
- Thorlabs AC300-100-A (achromatic doublet)
- Commercially available Zeiss grating

Several manufacturers, including Teledyne, ON Semiconductor, and Excelitas, can produce custom linear arrays with the necessary readout speed. Figure 25 illustrates one configuration of a 1U spectroradiometer that uses these components.

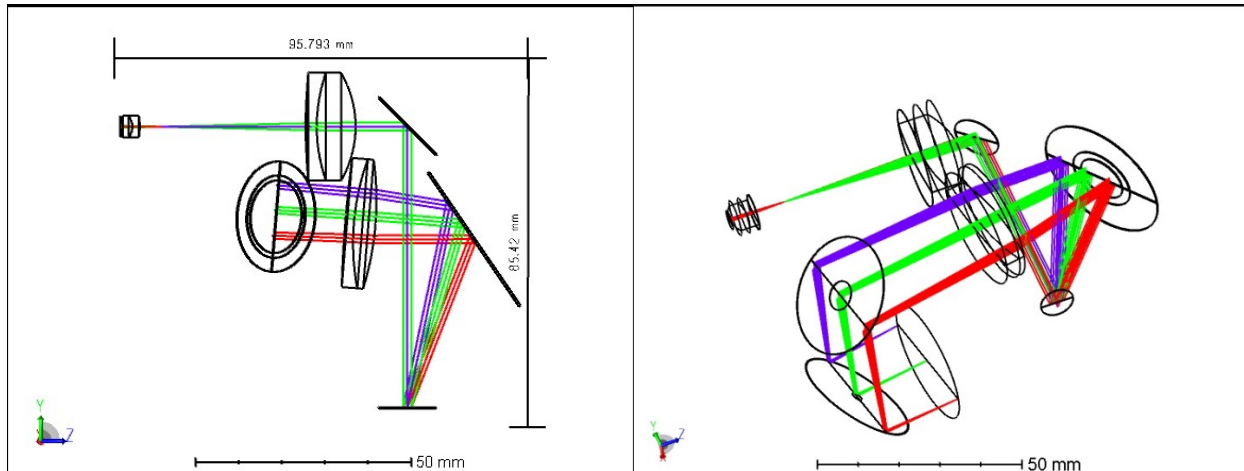


Figure 25. Volume ray trace model to verify the spectroradiometer can fit into a 1U compartment of a CubeSat.

4.3.3.2 Measuring the Sun-moon echo

Any high-cadence intensity fluctuations of the sun measured directly from the Earth may be caused by atmospheric fluctuations, including high altitude clouds, so it would be challenging to confirm the origin of fluctuations by simply staring at the sun. However, by simultaneously measuring sunlight scattered by the sky and light from the moon, we believe it may be possible to identify a sun-moon echo, if one exists. Because the position of the moon is well-known, the time delay can be determined by the relative Earth-Sun-Moon positions. The study we conceived is as follows:

1. A telescope is aimed at the moon during the day, when there is still diffuse sky radiation from the sun. Light collected from both the moon and atmospheric scatter passes through a blue filter, which passes the spectral band which is most scattered by Earth's atmosphere (thus maximizing the ratio of atmospheric scatter to moon reflection), and finally is received by a single photodiode.
2. The received signal is then digitized and recorded.
3. The fractional difference of the autocorrelation function at the time of sun-moon echo over the noise background represents the noise associated with an echo

The test is illustrated in Figure 26. Unfortunately, bad weather prevented us from testing the system until late in the program, but we did manage to acquire one data set with ~300,000 data points. The data from this measurement is shown in Figure 27. No signal was observed within the autocorrelation, but this is fairly reassuring because the sun is at an activity minimum, so any echo signal would be expected to be in the ppm level or lower, far below our present noise floor. Follow-on measurements with telescope tracking could provide additional bounds on the signal.

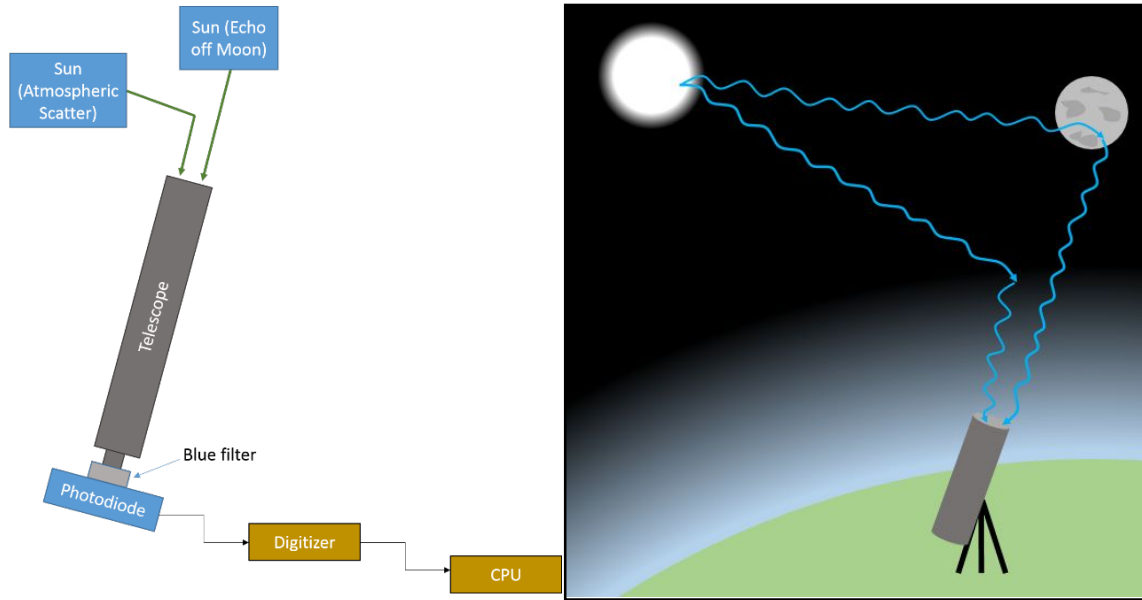


Figure 26. Schematic for the sun-moon echo experiment.

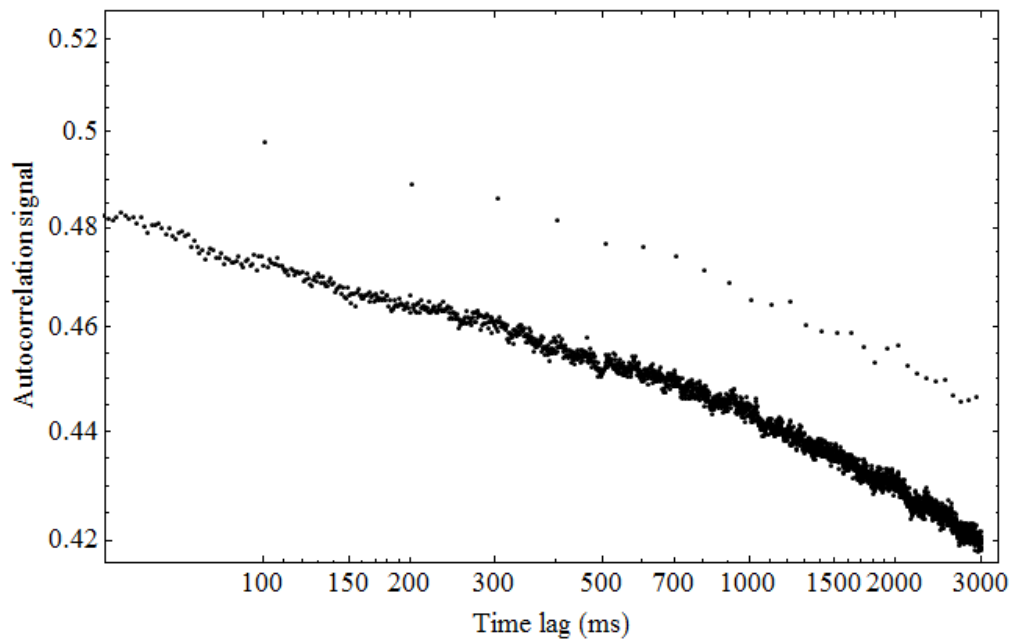


Figure 27. Sun-moon echo data. A digital readout noise source is likely responsible for the spurious peaks in the autocorrelation. At the time of month that the data was acquired, the echo would occur at ~300ms, but no signal is identifiable within the noise level.

4.3.4 Study of terrestrial planet imaging missions

The purpose of stellar echo techniques is to take advantage of the spatial resolution associated with temporal fluctuations of stars. With sufficient temporal accuracy, ~10ms, resolutions on the order of continents become attainable. However, this does not solve the problem of collecting and differentiating the photons from the planet from those of the star, which remains a significant signal-to-noise problem. In general, the solution to this problem is to exclude the light from the star using a coronagraph. While the preceding work on stellar echo measurements has primarily highlighted the power of ignoring the impressive technological

developments in direct imaging, we acknowledge that these two techniques may be most powerful when working together.

As a stand-alone methodology, stellar echo techniques can provide survey-level detection of exoplanets, and possibly their moons, that are presently undetectable by any existing technique. When utilized in a constellation, they can provide 3D correlation tomography of distant star systems, recreating the full 3D distribution of light-reflecting structures. But when coupled with emerging direct imaging technologies, including high-contrast coronagraphs for space telescopes, they could identify sub-structure in exoplanets with continent-level resolution without requiring multi-km, optically-flat baselines. Table 6 provides examples of the requirements for terrestrial planet imaging, which is presently an intractable problem. While these requirements are certainly challenging, modern coronagraphs are starting to demonstrate 10^9 level contrast,[29-31] making stellar-echo-enhanced direct imaging techniques viable.

Table 6. Preliminary values for a dedicated telescope within a terrestrial planet imaging constellation using a 200nm wide VIS-band filter, 70% combined telescope and detector quantum efficiency, and a 20m space telescope, and assuming the planet is viewed in quadrature.

Imaging goal	Star mag	Time between flares	Flare magnitude	Coronagraph contrast	Planet albedo	Planet distance (AU)	Feature/star contrast	Time for 1-sigma
$R_{\text{Earth}}/4$ features on Proxima b	11.13	31hr	100%	10^8	0.35	0.05	$\sim 10^{-9}$	9.7 days
R_{Earth} features in habitable zone of Lacaille 8760	6.7	27hr	10%	10^8	0.35	0.015	$\sim 10^{-9}$	7.2 days
Earth-like planet in an Earth-like orbit of a cooperative star	10	8hr	10%	10^9	0.35	1.0	$\sim 10^{-10}$	550 days

There is still certainly more work to go into the development of imaging Earth-like exoplanets, but these order-of-magnitude estimates show that timescales that are becoming common in space telescope operations could be used to resolve features of Earth-like exoplanets when combined with next-generation direct imaging approaches. And because any direct imaging mission that can isolate the point of light generated by a single exoplanet will have considerable angular resolution, it will likely be able to differentiate the position on the star that fluctuations are generated at, and can be used to better isolate the exoplanet’s signal. Utilizing the residual starlight, instead of throwing it away completely, may prove to be the last key to unlocking the mysteries of other worlds.

4.4 Laboratory studies

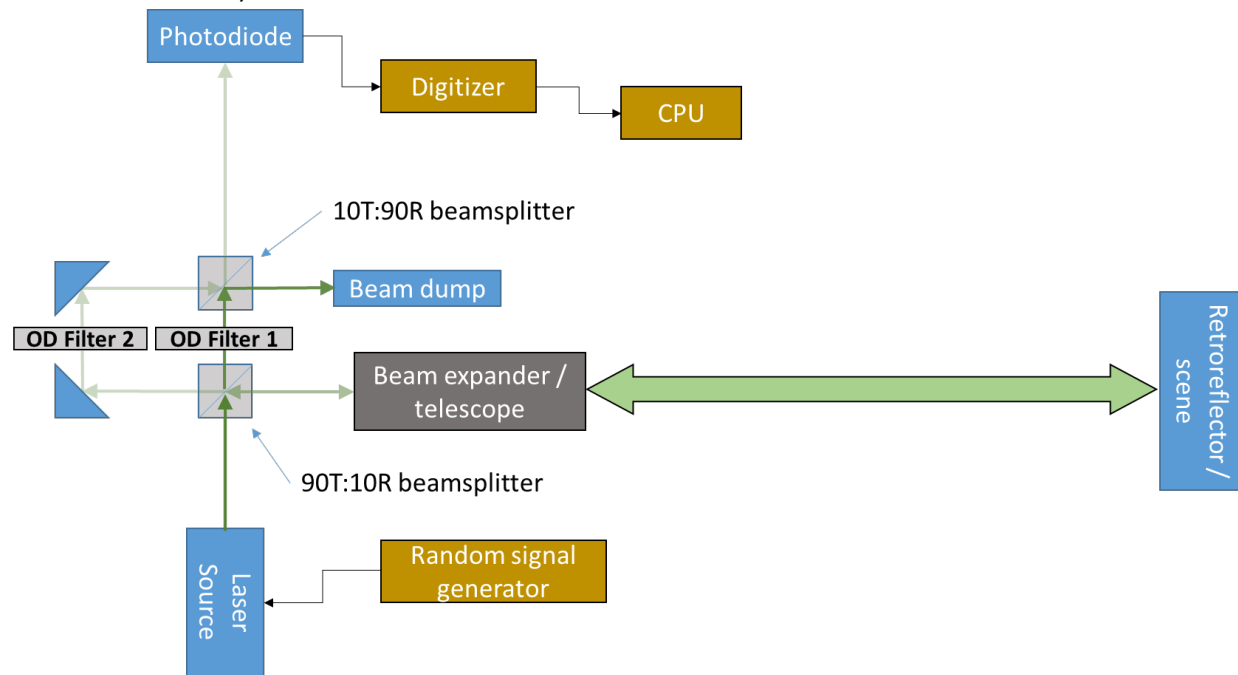


Figure 28. Design to evaluate a random-noise correlation detector.

Initially, we evaluated a hardware demonstration of random noise lidar systems, where we can generate different types of noise, project it onto a scene, then combine it with the original source light and perform an autocorrelation. Figure 28 illustrates the current design, where a random signal generator that can provide different magnitudes of noise is modulating a laser. The noise-modulated laser is then split into two paths: one path is the projection of the laser onto a scene, likely a retroreflector, positioned at ~1km away, to represent the exoplanet. The second path is passed through an OD filter to select how much light is obtained, then passed onto the photodiode. The return light from the retroreflector is passed through a separate OD filter that allows tuning of the star/planet contrast, which is then recombined with the original beam and passed onto the photodiode. Therefore, the photodiode receives both the initial signal and the echo-delayed signal. The total signal is digitized and passed onto a computer for correlation processing.

We stopped working on this demonstration when we became aware that random noise lidars are studied regularly, with a history going back to at least 1983.[32] In many ways, the established validity of random noise lidars provides substantial credibility to the stellar echo technique. The key advantage of random noise lidar is that the autocorrelation function of white noise is a delta function, which provides significant advantages over the sinc-shaped pulses traditionally used, including continuous operation. It has a broad bandwidth that reduces the noise, as well, by essentially multiplexing many channels simultaneously.

5 In Conclusion

Stellar echo detection, tomography, and imaging techniques represent a largely untapped source of high-resolution astronomy data. It is admittedly satisfying that there appears to be a viable class of solutions that beat the diffraction limit by exploiting previously deleterious stellar properties, including noise and residual coronagraph light. We hope that, even if the approaches pursued in this program are found to be impractical, the concepts explored here can help advance the ultimate goal of directly resolving worlds outside our solar system.

6 Acknowledgements

I am indebted to dozens of people for their discussions, insights, criticism, and support throughout the program. While they tried their best to share insights, any residual mistakes discovered in the report are entirely my own. Specifically, I want to thank the other 2016 NIAC Fellows for several fruitful discussions, as well as the NASA NIAC program for supporting this research. I am grateful to the entire CoRoT team, and while I didn't get a chance to speak with anyone directly, the data their satellite produced provided the first realistic processing and analysis conditions for the technique. I am grateful to Ed Nelan for the discussions, as well as the data from the Hubble Space Telescope Fine Guidance Sensor, which provided real-world, high-cadence, high-quality data to practice algorithms on. Thanks to the numerous people I ~~harassed~~ discussed the program with at the National Solar Observatory, the Southwest Research Institute, NIST, NASA, NOAA, and Ball. Thanks to Professor Ben Bromley for the great discussions, as well—I discovered, only near the end of the program, that he had already published a manuscript on stellar echoes in the 1990's. Thanks to Scott Kenyon for the discussion of numerous stellar mechanisms of relevance to the program. And thanks to the whole Nanohmics team: a program like this would never have received this much support and encouragement in a proper corporate environment!

7 References

1. Cowan, N.B. and T.E. Strait, *Determining reflectance spectra of surfaces and clouds on exoplanets*. The Astrophysical Journal Letters, 2013. **765**(1): p. L17.
2. Rosenblatt, F., *A two-color photometric method for detection of extra-solar planetary systems*. Icarus, 1971. **14**(1): p. 71-93.
3. Borucki, W. and A. Summers, *The photometric method of detecting other planetary systems*. Icarus, 1984. **58**: p. 121-134.
4. Johnson, M. and B. Dunbar. *How many exoplanets has Kepler discovered?* 2017; Available from: <https://www.nasa.gov/kepler/discoveries>.
5. Strelakov, D.V., B.I. Erkmén, and N. Yu, *Intensity interferometry for observation of dark objects*. Physical Review A, 2013. **88**(5).
6. Fried, D.L., J. Riker, and B. Agrawal, *Signal-to-noise ratio limitations for intensity correlation imaging*. J Opt Soc Am A Opt Image Sci Vis, 2014. **31**(7): p. 1536-46.
7. Bromley, B.C., *Detecting faint echoes in stellar-flare light curves*. Publications of the Astronomical Society of the Pacific, 1992. **104**(681): p. 1049-1053.
8. Clark, R.E., *A search for extrasolar planets using echoes produced in flare events*, in *College of Science and Mathematics*. 2009, California State University, Fresno.
9. Sugerma, B.E., *Observability of scattered-light echoes around variable stars and cataclysmic events*. The Astronomical Journal, 2003. **126**: p. 1939-1959.
10. Bless, R., et al., *The Hubble Space Telescope high-speed photometer*. Publications of the Astronomical Society of the Pacific, 1999. **111**: p. 364-375.
11. Benedict, G., et al., *Interferometric Astrometry of Proxima Centauri and Barnard's Star Using HUBBLE SPACE TELESCOPE Fine Guidance Sensor 3: Detection Limits for Substellar Companions*. The Astronomical Journal, 1999. **118**(2): p. 1086.
12. Benedict, G.F., et al., *Photometry of proxima centauri and Barnard's star using HST FGS3*. The Astronomical Journal, 1998. **116**: p. 429-439.
13. Benedict, G.F., et al., *Proxima centauri, time resolved astrometry of a flare site using HST FGS 3*. Cool Stars, Stellar Systems and the Sun, 1998. **154**: p. 1212.
14. Benedict, G.F., et al., *Periodic low-amplitude variations in the brightness of Proxima Centauri*. Astronomical Society of the Pacific, 1993. **105**(687): p. 487-493.
15. Gilliland, R.L., et al., *Asteroseismology of the Transiting Exoplanet Host Hd 17156 With Hubble Space Telescope Fine Guidance Sensor*. The Astrophysical Journal, 2011. **726**(1): p. 2.
16. Walker, A.R., *Flare activity of Proxima Centauri*. Mon. Not. R. ast. Soc., 1981. **195**: p. 1029-1035.
17. Traub, W.A. and B.R. Oppenheimer, *Direct Imaging of Exoplanets*. Exoplanets, 2010: p. 111.
18. Bessell, M.S., *UBVRI Photometry II: The Cousins VRI System, its Temperature and Absolute Flux Calibration, and Relevance for Two-Dimensional Photometry*. Publ. Astron. Soc. of the Pac., 1979. **91**: p. 589-607.
19. Sheikh, S.I., et al., *Spacecraft Navigation Using X-Ray Pulsars*. Journal of Guidance, Control, and Dynamics, 2006. **29**(1): p. 49-63.
20. Emadzadeh, A.A. and J.L. Speyer, *Relative Navigation Between Two Spacecraft Using X-ray Pulsars*. IEEE Transactions on Control Systems Technology, 2011. **19**(5): p. 1021-1035.
21. Anglada-Escude, G., et al., *A terrestrial planet candidate in a temperate orbit around Proxima Centauri*. Nature, 2016. **536**: p. 437-440.
22. Cincunegui, C., R.F. Díaz, and P.J.D. Mauas, *A possible activity cycle in Proxima Centauri*. Astronomy and Astrophysics, 2007. **461**(3): p. 1107-1113.
23. Lurie, J., et al., *The Solar Neighborhood. XXXIV. A Search for Planets Orbiting Nearby M Dwarfs using Astrometry*. The Astronomical Journal, 2014. **148**(5): p. 91.
24. Dravins, D., et al., *Atmospheric Intensity Scintillation of Stars. I. Statistical Distributions and Temporal Properties*. Publ. Astron. Soc. of the Pac., 1997. **109**: p. 173-207.

25. Dravins, D., et al., *Atmospheric Intensity Scintillation of Stars. III. Effects for Different Telescope Apertures*. Publ. Astron. Soc. of the Pac., 1998. **110**: p. 610-633.
26. Waller, D., et al., *MOIRE Thermal Vacuum Structural Stability Testing*. 2015.
27. Oschmann, J.M., et al., *MOIRE: ground demonstration of a large aperture diffractive transmissive telescope*. 2014. **9143**: p. 91431W.
28. Kretzschmar, M., et al., *The effect of flares on total solar irradiance*. Nature Physics, 2010. **6**: p. 690-692.
29. Serabyn, E., D. Mawet, and R. Burruss, *An image of an exoplanet separated by two diffraction beamwidths from a star*. Nature, 2010. **464**(7291): p. 1018-20.
30. Foo, G., D.M. Palacios, and J. Grover A. Swartzlander, *Optical vortex coronagraph*. Optics Letters, 2005. **30**(24): p. 3308.
31. Shaklan, S., et al., *Survey of experimental results in high-contrast imaging for future exoplanet missions*. 2013. **8864**: p. 88641F.
32. Takeuchi, N., et al., *Random modulation cw lidar*. Applied Optics, 1983. **22**(9): p. 1382.